Icarus 408 (2024) 115815

Contents lists available at ScienceDirect

Icarus

journal homepage: www.elsevier.com/locate/icarus

Overview of a large observing campaign of Jupiter's aurora with the Hubble Space Telescope combined with Juno-UVS data

B. Palmaerts [a,b,*], D. Grodent [a], B. Bonfond [a], Z.H. Yao [a,c], R.L. Guo [a,d], J.-C. Gérard [a],
K. Haewsantati [a,e], G.R. Gladstone [f], T.K. Greathouse [f], V. Hue [g], J.D. Nichols [h]

[a] *Laboratory for Planetary and Atmospheric Physics, STAR Institute, University of Liege, Liege, Belgium*
[b] *Remote Sensing and Geodata Unit, Scientific Institute of Public Service, Liege, Belgium*
[c] *Key Laboratory of Earth and Planetary Physics, Institute of Geology and Geophysics, Chinese Academy of Sciences, Beijing, China*
[d] *Laboratory of Optical Astronomy and Solar-Terrestrial Environment, Institute of Space Sciences, School of Space Sciences and Physics, Shandong University, Weihai, Shandong, China*
[e] *Department of Physics, Mahidol Wittayanusorn School, Nakhon Pathom 73170, Thailand*
[f] *Southwest Research Institute, San Antonio, TX, USA*
[g] *Aix-Marseille Université, CNRS, CNES, Institut Origines, LAM, Marseille, France*
[h] *Department of Physics and Astronomy, University of Leicester, Leicester, UK*

ARTICLE INFO

Keywords:
Jupiter
Aurora
Ultraviolet
Magnetosphere
Juno

ABSTRACT

Between February and September 2019, Jupiter's ultraviolet aurorae were frequently observed during a large campaign of the Hubble Space Telescope (HST GO-15638). The campaign included approximately 10 visits around each of the perijoves of the Juno spacecraft orbits 18 to 22 around Jupiter. During this time, the solar activity was minimal, giving the opportunity to investigate auroral dynamics minimally driven by the solar wind. The main emission often appeared fainter than usually observed, particularly on the dawn side where the dawn arc was not always present. In contrast, emissions poleward of the main emission were dynamic, exhibiting polar bright spots, extremely bright flares and quasi-periodic flashes. Many other features are observed, such as dawn storms, long-standing secondary arc parallel to the main emission, injection signatures, transpolar arcs and bridges connecting the main emission to the polar emissions. HST high temporal and spatial resolutions enable the investigation of the dynamics of the auroral structures and substructures like beads within the main emission. Juno auroral observations are also combined with HST images to track conjugate auroral features in both hemispheres simultaneously. Finally, a splitting of the main emission into two narrow parallel arcs is highlighted for the first time.

1. Introduction

Jupiter's auroral emissions span most of the electromagnetic spectrum. They are routinely observed in the ultraviolet, infrared, radio and X-Ray domains (see the review by Badman et al. (2015)). All wavelengths provide valuable information, but here we concentrate on the ultraviolet (UV) auroral emissions. These emissions are produced by the radiative de-excitation of the H_2 molecules and H atoms previously excited by collisions with precipitating magnetospheric electrons (e.g., Bhardwaj and Gladstone, 2000; Gustin et al., 2012). They exhibit a variety of structures and intensities around each magnetic pole of the planet which reveals the complexity and diversity of processes taking place in the huge Jovian magnetosphere.

Initially detected by the two Voyager spacecraft (Broadfoot et al., 1979), extensive investigations of Jupiter's UV aurora really became possible in the 1990's based on the high-resolution observations provided by the cameras on board the Hubble Space Telescope (HST), as reviewed by Clarke et al. (2004). After several observing campaigns of the aurora over a couple of decades, the interest of HST observations became even higher when the NASA Juno spacecraft arrived at Jupiter in July 2016. Combining the in situ data provided by Juno and the remote sensing observations by HST helps to interpret both types of information. Furthermore, since Juno is also equipped with an ultraviolet spectrograph, aurorae can occasionally be observed in both hemispheres simultaneously, enabling the identification and tracking of conjugate emissions.

---

[*] Corresponding author.
E-mail address: b.palmaerts@uliege.be (B. Palmaerts).

https://doi.org/10.1016/j.icarus.2023.115815
Received 26 April 2022; Received in revised form 20 September 2023; Accepted 24 September 2023

Hence, some HST campaigns were scheduled to take advantage of Juno's presence in the Jovian environment. A first program (GO-14105) started a few weeks before Juno's orbit insertion (JOI) and ended shortly after JOI, providing a continuous monitoring of the interplanetary conditions upstream of the magnetosphere. The observations of this campaign were analyzed in Nichols et al. (2017a). A large set of auroral observations was also performed between November 2016 and September 2018. The main part of this program (GO-14634), described by Grodent et al. (2018), covers eight months between Juno's orbits 3 and 7, totaling 118 sequences of ~40-min long observations. From this large campaign, Grodent et al. (2018) defined six auroral morphological families, each of them tentatively associated with a particular magnetospheric state. A first family corresponds to a compressed magnetosphere induced by a solar wind event (family 'X' according to their nomenclature). The opposite state is associated with a quiet and undisturbed magnetosphere (family 'Q'). Two states are characterized by the presence of plasma injections (families 'I' and 'i'). A family corresponds to a post-injection phase of the magnetosphere returning to a quiet state ('N'). Finally, a magnetosphere releasing energy through plasma instabilities defines family 'U'. Nichols et al. (2019) also identified similar families through machine learning techniques.

The different magnetospheric states and their associated auroral morphology are the consequences of internal and external drivers. Inside the magnetosphere, auroral dawn storms are related to recurring magnetotail reconfigurations associated with the internally driven Vasyliunas cycle (Kimura et al., 2015; Yao et al., 2020; Bonfond et al., 2021). Moreover, changes of the Io plasma torus density and mass outflow rate can also leave a signature in the aurora (e.g., Bonfond et al.,

Table 1
List of HST visits during campaign GO-15638.

Index	Root name	HST time (dd/mm/yyyy hh:mm:ss)	HST DOY 2019	Juno time (dd/mm/yyyy hh:mm:ss)	Hemi-sphere	CML start [deg]	Fa-mily
c01	odxc01okq	09/02/2019 18:05:53	39.8	09/02/2019 17:18:09	N	148.0	N
c02	odxc02phq	10/02/2019 00:27:14	40.0	09/02/2019 23:39:32	S	18.5	U
c04	odxc04a1q	10/02/2019 21:06:39	40.9	10/02/2019 20:19:03	S	47.7	N
c03	odxc03agq	11/02/2019 00:17:21	41.0	10/02/2019 23:29:46	N	163.0	N
c05	odxc05f4q	11/02/2019 19:21:21	41.8	11/02/2019 18:33:52	N	134.5	N
c06	odxc06haq	12/02/2019 01:42:45	42.1	12/02/2019 00:55:18	S	5.1	I
PJ18		12/02/2019 18:21	42.8	12/02/2019 17:34			
c07	odxc07q5q	13/02/2019 20:37:47	43.9	13/02/2019 19:50:33	N	121.6	N
c08	odxc08q9q	13/02/2019 22:12:05	43.9	13/02/2019 21:24:51	N	178.6	N
c09	odxc09z4q	09/03/2019 11:54:25	67.5	09/03/2019 11:10:16	N	177.0	Q
c10	odxc10ccq	10/03/2019 06:59:16	68.3	10/03/2019 06:15:13	N	149.1	N
c11	odxc11ryq	28/03/2019 21:32:31	86.9	28/03/2019 20:50:57	N	147.0	Q
c12	odxc12w3q	29/03/2019 18:11:48	87.8	29/03/2019 17:30:21	N	176.2	U
c13	odxc13axq	30/03/2019 22:48:22	89.0	30/03/2019 22:07:05	N	134.0	U
c14	odxc14ekq	31/03/2019 19:27:05	89.8	31/03/2019 18:45:54	N	162.9	U
c15	odxc15fpq	01/04/2019 16:06:24	90.7	01/04/2019 15:25:20	N	192.1	U
c16	odxc16htq	02/04/2019 01:38:23	91.1	02/04/2019 00:57:22	N	177.9	i
c17	odxc17r5q	03/04/2019 17:21:45	92.7	03/04/2019 16:40:57	N	178.9	i
c18	odxc18zuq	05/04/2019 18:37:06	94.8	05/04/2019 17:56:33	N	165.6	U
PJ19		06/04/2019 12:54	95.5	06/04/2019 12:14			
c19	odxc19dwq	06/04/2019 15:16:26	95.6	06/04/2019 14:36:00	N	194.9	Q
c20	odxc20esq	06/04/2019 23:13:05	96.0	06/04/2019 22:32:41	N	123.0	U
c21	odxc21f7q	30/04/2019 03:19:12	119.1	30/04/2019 02:41:24	N	136.3	N
c23	odxc23qcq	22/05/2019 22:00:38	141.9	22/05/2019 21:24:30	N	169.0	X
c25	odxc25txq	23/05/2019 17:04:39	142.7	23/05/2019 16:28:33	N	140.8	X
c22	odxc22csq	25/05/2019 13:34:03	144.6	25/05/2019 12:58:02	S	314.8	U
c27	odxc27gdq	26/05/2019 14:59:27	145.6	26/05/2019 14:23:29	N	157.1	I
c24	odxc24heq	26/05/2019 21:20:48	145.9	26/05/2019 20:44:50	S	27.7	N
c26	odxc26eeq	27/05/2019 18:00:10	146.8	27/05/2019 17:24:14	S	57.0	N
c28	odxc28j4q	28/05/2019 21:00:56	147.9	28/05/2019 20:25:03	S	317.0	U
PJ20		29/05/2019 08:44	148.4	29/05/2019 08:08			
c29	odxc29n4q	29/05/2019 12:54:19	148.5	29/05/2019 12:18:27	N	173.5	I
c30	odxc30rdq	30/05/2019 17:30:24	149.7	30/05/2019 16:54:34	N	131.1	U
c31	odxc31dxq	14/07/2019 19:37:26	194.8	14/07/2019 19:00:32	N	146.5	N
c32	odxc32d6q	15/07/2019 14:43:55	195.6	15/07/2019 14:06:58	N	119.7	N
c33	odxc33dbq	15/07/2019 16:16:37	195.7	15/07/2019 15:39:39	N	175.7	U
c34	odxc34gqq	16/07/2019 11:20:30	196.5	16/07/2019 10:43:29	N	147.2	i
c36	odxc36poq	18/07/2019 14:10:54	198.6	18/07/2019 13:33:43	N	191.4	U
c37	odxc37ruq	19/07/2019 09:14:49	199.4	19/07/2019 08:37:34	N	162.9	N
c35	odxc35tlq	19/07/2019 18:46:47	199.8	19/07/2019 18:09:30	N	148.7	N
c38	odxc38xkq	20/07/2019 13:52:59	200.6	20/07/2019 13:15:38	N	121.7	X
PJ21		21/07/2019 04:39	201.2	21/07/2019 04:02			
c39	odxc39c7q	21/07/2019 10:30:00	201.4	21/07/2019 09:52:34	N	149.5	N
c40	odxc40n8q	04/09/2019 12:37:29	246.5	04/09/2019 11:54:59	N	157.4	U
c41	odxc41q5q	05/09/2019 07:41:21	247.3	05/09/2019 06:58:45	N	128.8	U
c42	odxc42ahq	07/09/2019 10:31:42	249.4	07/09/2019 09:48:50	N	172.6	Q
c43	odxc43edq	08/09/2019 15:07:32	250.6	08/09/2019 14:24:31	N	129.7	U
c44	odxc44efq	08/09/2019 16:42:51	250.7	08/09/2019 15:59:50	N	187.3	U
c45	odxc45dnq	09/09/2019 11:46:44	251.5	09/09/2019 11:03:36	N	158.7	i
c46	odxc46i8q	10/09/2019 05:15:20	252.2	10/09/2019 04:32:07	S	72.5	X
c47	odxc47itq	10/09/2019 08:26:00	252.4	10/09/2019 07:42:46	N	187.7	Q
PJ22		12/09/2019 04:23	254.2	12/09/2019 03:40			
c48	odxc48zuq	12/09/2019 09:41:10	254.4	12/09/2019 08:57:40	N	173.9	U
c49	odxc49e8q	13/09/2019 04:45:09	255.2	13/09/2019 04:01:33	N	145.3	I
c50	odxc50grq	13/09/2019 14:17:08	255.6	13/09/2019 13:33:29	N	131.0	Q

2012; Yoshikawa et al., 2017; Kimura et al., 2018; Tao et al., 2018). Outside, increases in the solar wind dynamic pressure trigger enhanced auroral activity (e.g., Nichols et al., 2017a; Kita et al., 2019; Yao et al., 2022).

The HST program GO-15638 described in the present manuscript took place between February and September 2019, close to the time of the minimum of the solar cycle 24 (December 2019). The observations provide the best opportunity to investigate the effects of internal processes minimally affected by the solar wind. Nonetheless, while coronal mass ejections are absent, solar wind events such as corotating interaction regions can still regularly hit Jupiter's magnetosphere, triggering an unambiguous auroral response. In the following, we review several global and local structures of Jupiter's aurora, as well as their dynamics, observed during the GO-15638 campaign.

2. Observations

The HST program GO-15638 consists of 50 orbits which include for most of them one single visit, i.e., one sequence of observation. Each visit is assigned an index which is the middle characters of the official HST archive root name (for instance, index "c01" for the root name "odx**c01**okq"). Table 1 gives information about each visit, namely the HST UT time at the start of the exposure, the same time converted in decimal day of year (DOY), the corresponding time at Juno taking into account the light travel time between HST and Juno, the hemisphere (North or South), Jupiter's central meridian System III (SIII) longitude (CML) at the start of the visit and the morphological family as defined by Grodent et al. (2018). The campaign is subdivided mainly into five periods of approximately one week, each occurring around Juno's perijoves (PJ) from orbits 18 to 22. The times of PJ18 to PJ22 are also listed in Table 1. A few visits were also performed close to Juno's apojove at the start of orbits 19 and 20.

Each HST visit provides an approximately 40 min-long continuous observation of one hemisphere of Jupiter. The observations are performed by the Space Telescope Imaging Spectrograph (STIS) UV camera, using the Far Ultraviolet Multi-Anode Microchannel Array (MAMA) and the Strontium Fluoride (SRF2) filter (∼130–182.5 nm) which excludes H Lyman-α contamination by geocoronal emission. The images were acquired in time-tagged imaging mode with an accumulation time of 10 s. Images presented hereafter have been integrated over 30 s to increase the signal-to-noise ratio. The STIS camera provides a platescale of 0.024 arcsec/pixel over a field of view of 25 × 25 arcsec^2.

The dark counts, flat field and geometry corrections were applied using the standard CalSTIS procedure from the Space Telescope Science Institute. Planetary disk background emissions were removed to isolate auroral emissions, following the method described by Bonfond et al. (2011). Count rates on the detector were converted to brightness and power emitted in the 70–180 nm range, using the conversion coefficients inferred by Gustin et al. (2012) and assuming a typical colour ratio of 2.5. HST images presented here are projected on a polar map fixed in System III (as illustrated in Fig. 1), after applying the limb fitting procedure described by Bonfond et al. (2009) and considering an auroral emission altitude of 400 km (Bonfond et al., 2015b). For the southern hemisphere, the projections are oriented so that the aurorae are seen through the planet from above the north pole.

To complement HST observations, observations from Juno's Ultraviolet Spectrograph (UVS) are presented in this manuscript. Juno-UVS is an imaging spectrograph operating in the 68–210 nm range (Gladstone et al., 2017). The nominal orientation of the slit is perpendicular to the spacecraft rotation axis, however an adjustable mirror at the entrance of the instrument allows it to point up to 30° away from the rotation plane. The slit has a dog-bone shape, and only the 0.2°-wide sides of the slit are used in this study for a better signal-to-noise ratio. Moreover, in this work, the wavelength range was limited to 155–162 nm, in order to avoid areas of the H_2 spectrum affected with hydrocarbon absorption. This brightness is then multiplied by 8.1 in order to compute the total H_2 UV brightness in 4π steradians (Gustin et al., 2012). For each photon detection event, the intersection the pixel's field of view and an ellipsoid located 400 km above Jupiter's 1-bar level is computed. An image of the auroral UV emissions is progressively constructed for each Juno spin. Consecutive partial images of the aurora, acquired for different mirror positions, are then assembled to produce more complete maps. Additional discussions of the calibration, uncertainty sources and background subtraction can be found in Greathouse et al. (2013), Hue et al. (2019a, 2021b), Gérard et al. (2020) and Bonfond et al. (2021).

Jovian auroral emissions can be divided into three subregions defined in Nichols et al. (2009b) and Grodent et al. (2018). These subregions, highlighted in the right panel of Fig. 1, include a ribbon encompassing the main emission, the region poleward of the main emission, also called the polar or poleward region, and the equatorward region bounded by the equatorward boundary of the main emission ribbon. The main emission ribbon is built from one of the main emission reference contours derived in Bonfond et al. (2012), selecting the contour which fits the best the observed main emission. The width of the

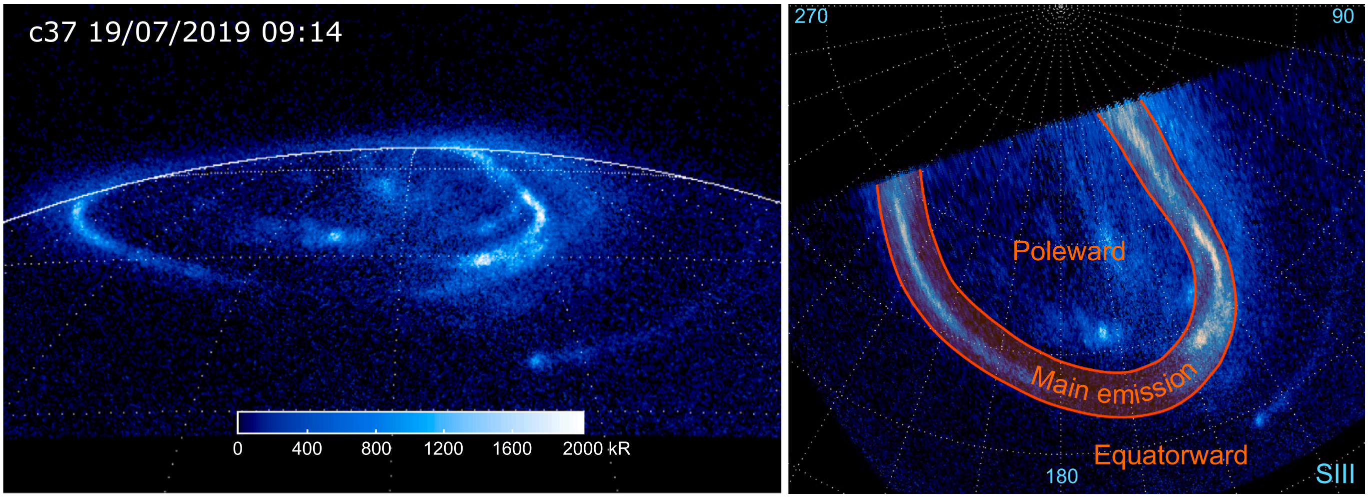

Fig. 1. Left: Example of an HST/STIS UV observation of the northern Jovian aurora acquired during the GO-15638 campaign. The emissions have been accumulated over 30 s and the colour scale is saturated at 2000 kR. The white line indicates Jupiter's limb. Right: The same image projected on a polar map with 10°-spaced System III meridians and parallels. The main emission region, separating the poleward and the equatorward emissions, is highlighted in orange. (For interpretation of the references to colour in this figure legend, the reader is referred to the web version of this article.)

ribbon is set to 5.0° on the surface of Jupiter. The equatorward subregion is magnetically connected to the inner magnetosphere where the Galilean moons are located ($<\sim 20$ R_J, where 1 $R_J = 71{,}492$ km), while the poleward subregion is linked to the outer magnetosphere ($> \sim 40$ R_J).

Figure 2 shows the auroral power emitted in each subregion (the main emission in red, the poleward emissions in green and the equatorward emissions in orange) for all the HST observations acquired around Juno's perijoves 18 to 22. The auroral power was corrected for the viewing geometry, as explained in Grodent et al. (2018). Only the median power value is given for each visit and subregion, but the power can vary on short timescales within a visit, for instance, when a bright flare appears in the polar region (see Section 4).

The auroral power remained most of the time (74% of the observations) below 600 GW within each subregion, with a total power ranging between 0.8 and 1.4 TW. However, Fig. 2 reveals that large power enhancements sometimes occur in a subregion. The power can increase by a factor of 2–3 in the main emission ribbon due to dawn storms ("DS", c17, c29, c45, c49, see Sections 3.2 and 3.3) or brightening of the narrow dawn arc ("DA", c23, c25, Section 3.4). The presence of extended quasi-periodic flares ("QPF") can increase the median power in the polar region, e.g., in visit c30 (Section 4). The power emitted in the equatorward subregion is enhanced, up to 1 TW, when injection signatures are present ("I", c06, c26, c40, c45, Section 5.1) or when the Io's auroral footprint is brighter ("IFP", c24, Section 5.2). Finally, all auroral emissions can also brighten as a whole (Global Brightening "GB", Section 3.4), like in visit c46 when the total auroral power reached 3 TW, the maximal value of the campaign.

As suggested by Fig. 2, observations acquired near Juno's perijove 22 (PJ22, 12 September 2019) exhibit many remarkable phenomena. These observations are displayed in Fig. 3, with one image selected for each visit between September 4 and September 13. Several auroral structures are highlighted and are discussed in the following sections. Sections 3, 4 and 5 are devoted to the main emission, the polar emissions and the equatorward emissions, respectively.

3. Main auroral emission

The main auroral emission generally forms a discontinuous strip of emissions around the magnetic pole (like in Fig. 1). Its general morphology remains relatively stable and is fixed in SIII longitudes (Grodent et al., 2003b). The main emission exhibits a marked dawn-dusk asymmetry as observed from HST with a narrow arc in the dawn sector and more diverse and less defined emissions in the post-noon and dusk sectors. Between these two distinct parts of the main emission, its brightness often drops due to faster plasma rotation in the prenoon sector, forming the so-called discontinuity around noon local time (Radioti et al., 2008, Chané et al., 2013). A small-scale auroral spot can occasionally be present at the duskward edge of the discontinuity and is attributed to an ultralow-frequency wave process or to shearing motions resulting from intermittent inward radial plasma flow (Palmaerts et al., 2014, Nichols et al., 2017b, Chané et al., 2018). In the southern

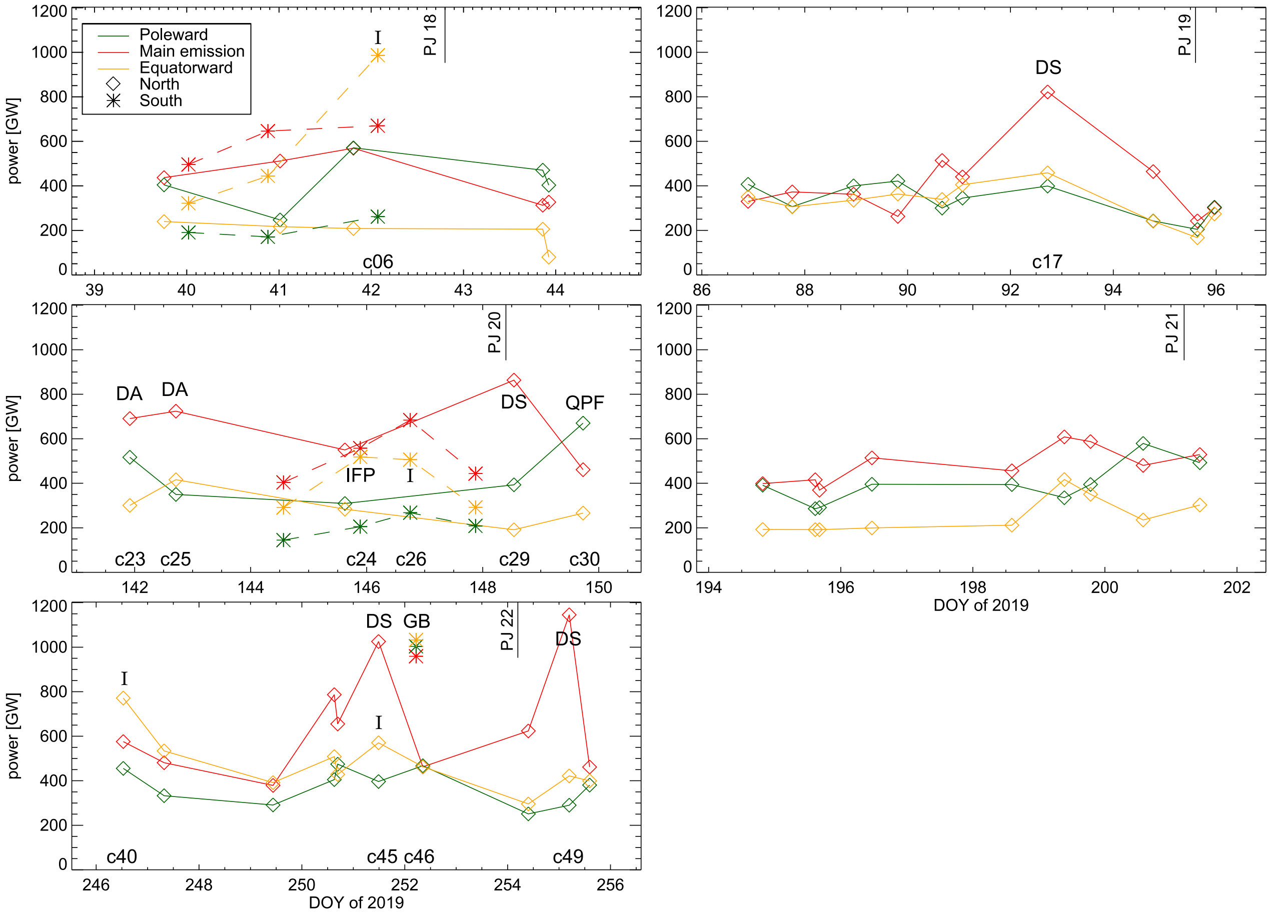

Fig. 2. Median auroral power emitted by the poleward emissions (green), the main emission (red) and the equatorward emissions (orange) for each HST visit of the GO-15638 campaign. Diamond symbols connected by a solid line indicate the observations in the northern hemisphere, while southern aurora observations are represented by stars connected by a dashed line. Each subpanel covers a time interval around Juno's perijove 18 to 22, whose times are indicated by vertical lines. The time is given in day of year (DOY) 2019. The index of some of the visits mentioned in the text are indicated. (For interpretation of the references to colour in this figure legend, the reader is referred to the web version of this article.)

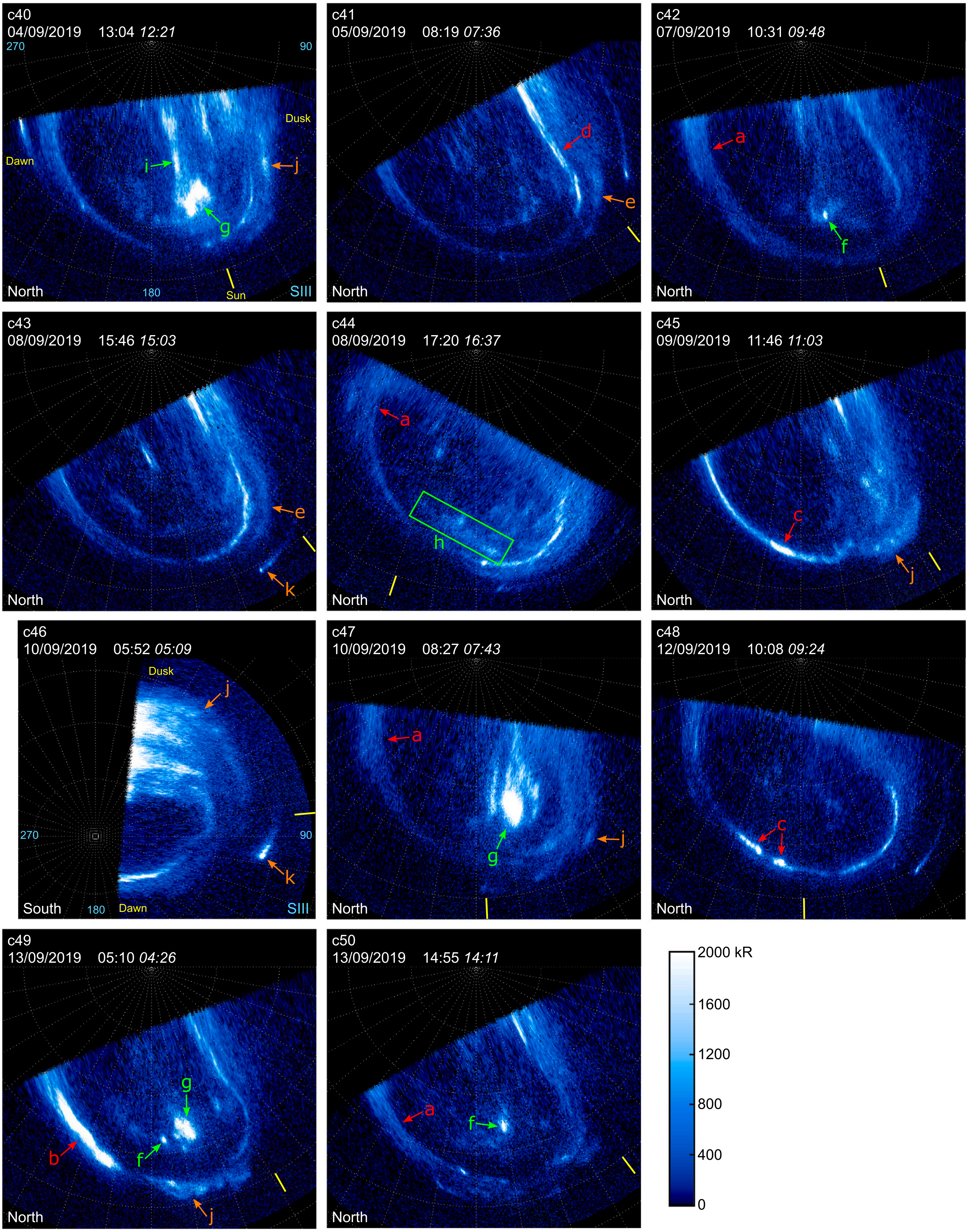

Fig. 3. HST-STIS observations of Jupiter's aurora during 10 days in September 2019, near Juno's perijove 22 (September 12 at 04:23 UT, HST time). The auroral emissions are projected like in Fig. 1. The visit index, the HST UT time and the Juno UT time (in italic) of the observations are indicated on top of each panel. A yellow line indicates the longitude facing the Sun (12 LT). Several auroral structures are highlighted and discussed in the text: features a, b, c, d, e in Section 3; features f, g, h, i in Section 4; features j, k in Section 5. (For interpretation of the references to colour in this figure legend, the reader is referred to the web version of this article.)

hemisphere, the main emission has an oval shape, while the northern main emission is distorted due to a magnetic anomaly around 100° SIII longitude (Grodent et al., 2008; Connerney et al., 2018). Given the geometry of observation from the Earth orbit, this distortion is always located around dusk on HST northern auroral observations.

3.1. *Faint dawn main emission*

In the dawn sector, the main emission usually forms a clear arc at the boundary between the polar dark region and the diffuse outer emissions. In this campaign, this arc was often particularly faint, and even sometimes not visible on the auroral images, as pointed by the red arrows with the letter ‘a’ on Fig. 3. While the brightness of the main emission is usually lower at dawn than at dusk (Bonfond et al., 2015a), the absence of a dawn arc as reported here was not frequently observed in previous observing campaigns (Nichols et al., 2017a). HST does not provide a continuous observation of the aurora, however this faint main emission at dawn was consistently observed during several consecutive visits, suggesting that its brightness could remain low over several days.

The dim dawn arc could be related to the low solar activity and a generally expanded magnetosphere (Nichols et al., 2017a). We surveyed this faint emission in the previous HST campaigns and compared its occurrence with the number of sunspots observed on the solar surface, which is the traditional indicator of the solar activity. No clear correlation emerged from this comparison but the investigation of the correlation is hampered by the limited number of observing days during the solar maxima of cycles 23 and 24.

3.2. *Dawn storms*

During a period of faint main emission at dawn, some powerful events can nevertheless affect it, such as a dawn storm. A dawn storm occurred on September 13, consisting of a large and bright structure observed on visit c49 (Fig. 3, feature b), whereas the emission was particularly weak 3 days earlier (c47), one day earlier (c48) and 9.5 h later (c50). This dawn storm was present during the whole ∼40-min observing time of visit c49 and its structure started to fragment longitudinally into three parts, as often observed (Bonfond et al., 2021). Combining HST observations with simultaneous Juno in situ data, Yao et al. (2020) and Swithenbank-Harris et al. (2021) showed that magnetotail reconnection or possibly current disruption generates dawn storms.

Another dawn storm was observed during the campaign, on May 29 (c29). Top panels of Fig. 4 display two snapshots of the dawn storm separated by 20 min. Again, the bright structure divided into two parts separated by a growing longitudinal gap. This dawn storm was observed by HST in the northern hemisphere. Simultaneously, the Juno spacecraft was flying over the southern polar region (PJ20) with its UVS instrument acquiring images of the southern aurora. Some UVS images are reproduced on the bottom panels of Fig. 4. HST and UVS data are chronologically sorted from left to right and the same polar map orientation is used for all panels, enabling a direct comparison of the auroral features in both hemispheres. The southern aurora exhibits an obvious dawn storm as well. The longer UVS observing period captures the evolution of the southern dawn storm from its birth until it became fragmented like the northern storm. Hence, the synergy between Juno-UVS and HST provided clues that conjugate dawn storms evolve similarly in both hemispheres.

3.3. *Beads*

The time-tag observations also reveal dynamics within the thin dawn arc of the main emission. At the start of visit c48, a bright auroral spot, fixed in System III, was located at around 185° longitude (pink arrow on top row of Fig. 5). Then, a second spot developed at ∼195° (orange arrow) and grew by the merging of a succession of tiny spots (red arrows), like beads, coming from higher longitudes. A movie of the whole visit is provided in the supplementary material (Movie S1). The opposite process was observed during visit c45, where an elongated bright spot at the same longitude as in the first sequence (middle row of Fig. 5, orange arrow) split in several smaller spots (red arrows, Movie S2). Visit c17 also shows a dynamic dawn arc in which the section between 208° and 223° longitude became visible after the appearance and merging of a couple of arcs which intensified to reach a peak brightness of 9 MR after 32 min (bottom row of Fig. 5 and Movie S3).

Juno-UVS observations of the southern aurora concomitant with the c48 visit reveal a patchy and bright emission at the same longitude as the dynamic main emission arc. However, the temporal and spatial resolutions of UVS prevent from following the dynamics within the patchy emission in the southern hemisphere. The motion of the beads observed

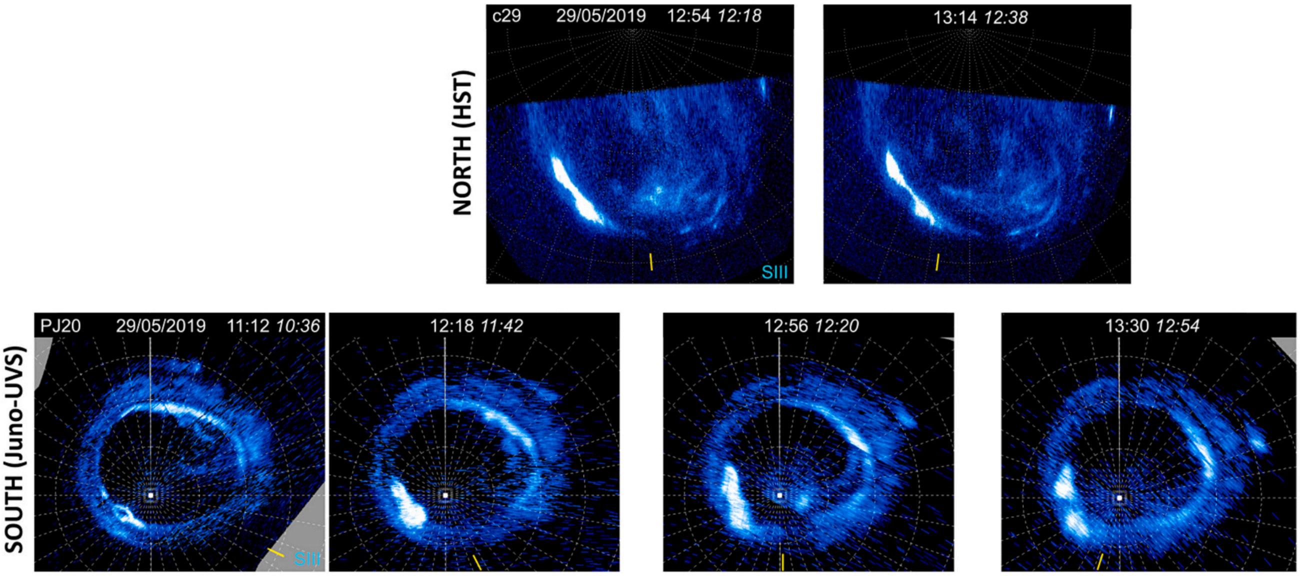

Fig. 4. Conjugate observations of the evolution of a dawn storm in the northern hemisphere captured by HST and in the southern hemisphere captured by Juno-UVS during PJ20. The observing sequence is going from left to right, with the HST UT time and Juno time (in italic) indicated for both HST and Juno observations. The yellow line marks the subsolar longitude. (For interpretation of the references to colour in this figure legend, the reader is referred to the web version of this article.)

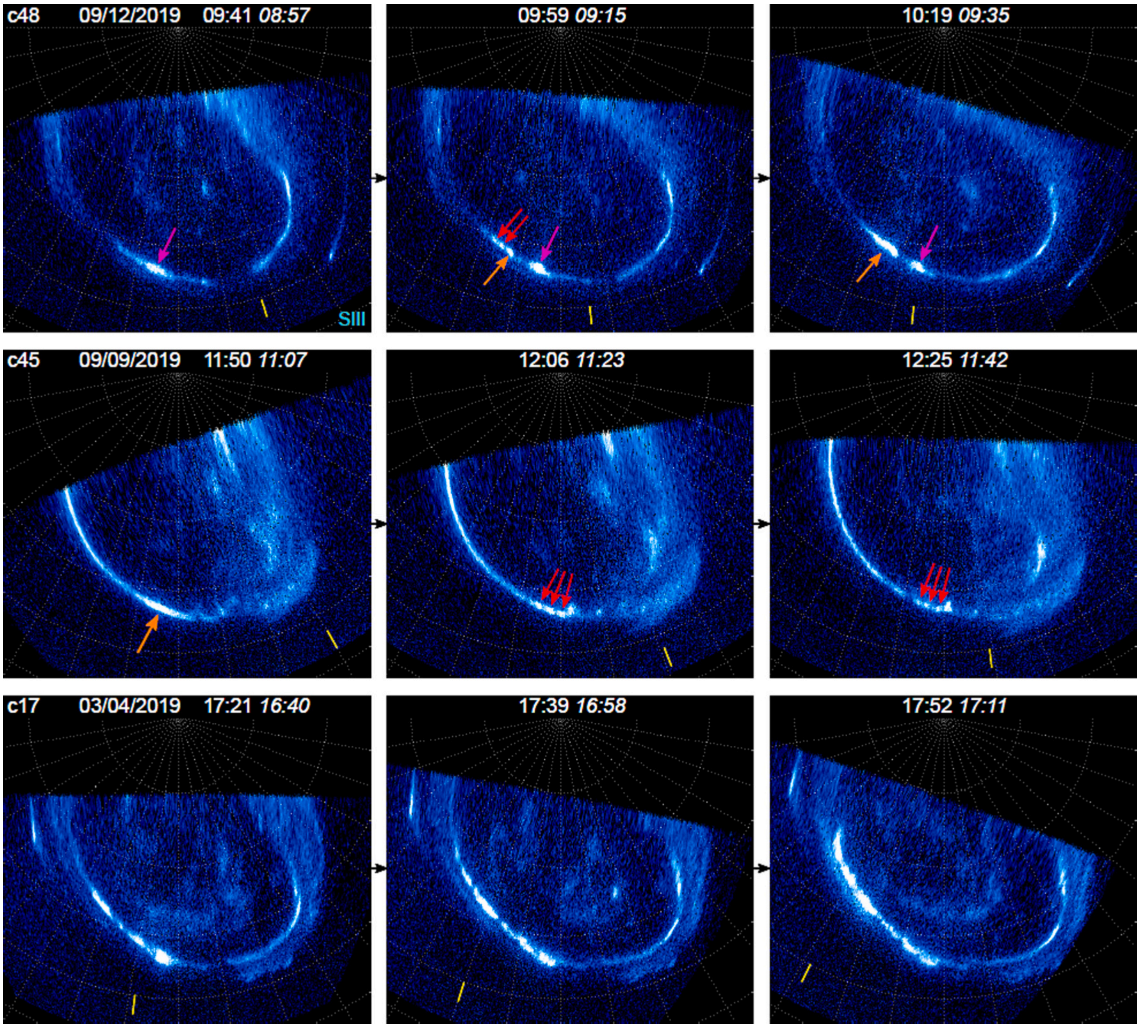

Fig. 5. Three auroral sequences showing the formation of beads (red arrows) in the dawn section of the main emission. The pink arrows point to a relatively unvarying spot fixed in System III. The orange arrows point to the spot resulting from the bead merging or splitting into beads. The HST UT time and the Juno UT time (in italic) of the observations are indicated on top of each panel. The yellow line points to the Sun. (For interpretation of the references to colour in this figure legend, the reader is referred to the web version of this article.)

in the northern hemisphere might be a signature of plasma instabilities in the plasma sheet, such as ballooning instability (e.g., Pu et al., 1997; Yao et al., 2017). The relation between auroral beads and magnetospheric instabilities has been already highlighted at Saturn (Radioti et al., 2019) and at Earth (e.g., Rae et al., 2010; Kalmoni et al., 2015). The beads at Jupiter might also correspond to the Saturnian auroral patches associated with a rotating multiple field-aligned current structure (Guo et al., 2021). Further investigation using Juno in-situ measurements are necessary to find out their driving process. The initial steps of the Jovian dawn storm process include the emergence of auroral beads (Bonfond et al., 2021). These pre-storm beads are found in the midnight-to-dawn sector, contrary to the beads reported here. However, the bright emissions in the prenoon sector observed in the three examples of Fig. 5 are similar to pseudo-dawn storms, which are a kind of not fully developed dawn storms (Bonfond et al., 2021).

3.4. Solar wind influence

Observations have shown that the occurrence of dawn storms is independent of the solar wind conditions (Nichols et al., 2009b; Bonfond et al., 2021). This independence is in agreement with an internally-driven origin, such as reconnection (Kimura et al., 2017; Yao et al., 2020; Swithenbank-Harris et al., 2021). However, solar wind shocks compressing the magnetosphere can cause a large enhancement of the intensity of the main emission dawn arc or even a global brightening of the whole dayside main emission (Nichols et al., 2007, 2009b, 2017a; Grodent et al., 2018; Yao et al., 2022). A bright narrow dawn arc was observed twice during this campaign, in May (c23 and c25) and in September in both hemispheres (c45 and c46, Fig. 3). During c46, the dusk aurora and the Io auroral footprint (feature indicated by a ‘k’ in Fig. 3) were also particularly bright. Large injection signatures were also present (feature j). The next visit (c47) shows that the main emission recovered low intensities at all local times only 2.5 h later, with a total auroral power decreasing from 3 TW to 1.4 TW.

Juno being close to perijove, no direct or indirect measurements of the upstream solar wind (SW) parameters are available during c45/c46. Hence, we must rely on solar wind propagation models from the Earth to Jupiter to estimate these parameters. The model by Tao et al. (2005) is a one-dimensional magnetohydrodynamic (MHD) model using near-Earth solar wind measurements as input parameters. Its prediction accuracy is at most two terrestrial days when the Earth-Sun-Jupiter angle does not exceed 50°. Fig. S1 in the Supplementary Material shows the estimated SW dynamic pressure around each of the perijoves 18 to 22. Tao’s model predicts a sharp increase of the dynamic pressure at Jupiter on September 8, revealing the arrival of a SW shock which compressed Jupiter’s magnetosphere. On that day, the Earth-Sun-Jupiter angle is around 63°, implying that the inaccuracy on the shock arrival time can exceed two days. Nevertheless, a SW shock on September 8 is compatible with the auroral global brightening observed the next two days in both hemispheres (c45 and c46 on Fig. 3) since the auroral response is expected 10–15 h after the shock hit the magnetopause (Kita et al., 2019).

Additionally, we examined the predictions of the ENLIL tool which is a three-dimensional MHD model of the heliosphere (Odstrcil, 2003; Odstrcil et al., 2004). ENLIL generates a background solar wind from 0.1 AU to 10 AU based on a coronal model which uses photospheric magnetic field observations. On top of the background solar wind, disturbances such as Coronal Mass Ejections (CMEs) are propagated with properties derived from coronagraph observations. The ENLIL simulation shows a corotating interaction region (CIR) reaching Jupiter in the afternoon of September 8 (Fig. S2 right), in agreement with Tao’s model.

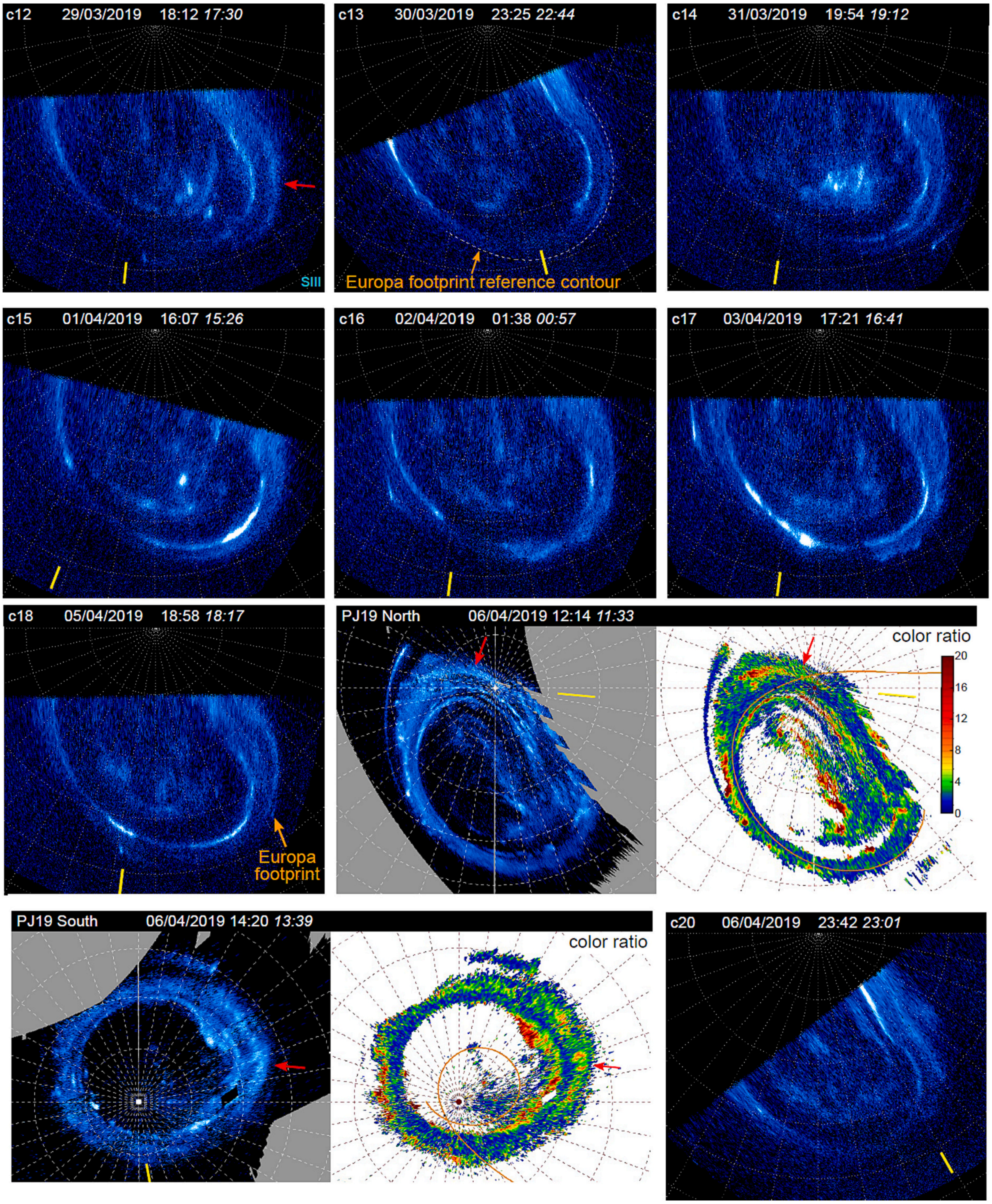

Fig. 6. Sequence of HST and Juno-UVS observations showing a secondary arc at dusk parallel to the main emission (red arrows). The HST UT time and the Juno UT time (in italic) are indicated for HST and Juno observations. The yellow line points to the Sun. The Europa footprint reference contour (Bonfond et al., 2017c) is drawn with a dashed line on the polar projection c13. The Far-UV colour ratio maps associated with the UVS images are also shown. (For interpretation of the references to colour in this figure legend, the reader is referred to the web version of this article.)

Finally, both solar wind propagation models indicate a relatively weak CIR arriving at Jupiter a few hours before the observation of a bright main emission dawn arc on visit c23 and c25 on May 22 (Fig. S1 and S2 left).

3.5. *Secondary arc*

A secondary arc is sometimes observed at lower latitudes than the main emission and at various longitudes (Grodent et al., 2003b; Gray et al., 2017). Although being part of the equatorward emission region, its morphology links it to the main emission. This long and narrow structure is roughly parallel to the main emission and is fainter (feature e in Fig. 3). The secondary arc was suggested to result from electron scattering caused by wave-particle interactions at the boundary between two electron pitch angle distributions (Tomás et al., 2004; Gray et al., 2017). Fig. 6 displays an observing sequence covering 8 days between March 29 and April 6. The first four visits (c12 to c15) show that a secondary arc was present in the noon-to-dusk sector during four consecutive days. In c15, the presence of the secondary arc is only visible between 160° and 175° of longitude whereas the equatorward emissions are more diffuse at lower longitudes. The secondary arc was then not clearly distinguishable during the next two visits (c16 and c17). It should be noted that the dusk main emission was reduced to a short arc in c16. Two days later, the visit c18 shows that the secondary arc appears again and was also present during the last visit of the sequence (c20). Like in the previous observations reported by Gray et al. (2017), the secondary arc lies slightly polewards from the contour of Europa's auroral footprint (derived by Bonfond et al. (2017c)), as shown by the dashed curve on the snapshot c13 of Fig. 6. This is also clearly seen on c18 where the Europa footprint is located next to the secondary arc.

Earlier on the day of visit c20, Juno-UVS observed the northern aurora before PJ19 and the southern aurora afterwards. Because of the viewing geometry of HST from Earth orbit, it is not possible to disentangle whether the secondary arc in the northern aurora appears in a fixed local time sector or in a fixed SIII longitude range, noon local time being most of the time located between 120° and 210°. Juno provides an answer by capturing aurora at all local times and SIII longitudes independently. The UVS northern auroral image in Fig. 6 shows an arc parallel to the main emission on the dusk side at longitudes of around 45° and close to the pole (red arrow), which would not be visible with HST. This parallel arc is found in the dusk region as was the case on all HST images. Hence, the secondary arc can be observed at different local times and has a varying longitudinal extent (Gray et al., 2017), but once appeared, its local time position remains roughly fixed.

The secondary arc is more distinguishable on the colour ratio map (Fig. 6). The Far-UV colour ratio is the ratio between the total H_2 intensity in the 155–162 nm range, a wavelength domain not absorbed by methane, and the total intensity of the partly absorbed H_2 between 126 and 130 nm. This ratio is related to the energy of the precipitating electrons, since electrons with higher energy penetrate deeper into the hydrocarbon layer, implying a stronger absorption and thus a higher colour ratio (e.g., Yung et al., 1982; Gérard et al., 2016). The secondary arc appears as a region with a colour ratio somewhat lower than the colour ratio of the main emission at dusk. The UVS observation acquired a couple of hours later in the southern hemisphere shows also a secondary arc at dusk.

3.6. *Splitting of the main emission*

A particular phenomenon inside the main emission was detected for the first time during this campaign. Twice, a part of the main emission appeared split into two narrow parallel arcs separated by a thin gap filled with background level emissions (Fig. 7 and feature 'd' in Fig. 3). The gap is not present at the start of the sequence but gradually develops throughout the observing time. This phenomenon has not been reported in the previous observing campaigns and remains unexplained. The identification of the splitting did not occur during the Earth-Jupiter opposition time (June 2019) and thus does not result from a higher resolution of the auroral observation by HST/STIS. Juno's observations revealed that the main emission exhibited the same double arc structure the day before the occurrence on visit c07 (right panel of Fig. 7), indicating a rather long-lived structure. Juno observations show also that this structure, when it is present, is always found at similar longitudes, in the magnetic anomaly region (Grodent et al. 2008, Connerney et al., 2018), but can appear at different local times.

4. Polar emissions

The polar aurora, bounded by the main emission (Fig. 1), encompasses dynamic emissions with various timescales. It may be divided into three subregions: the dark, active and swirl regions (Grodent et al., 2003a). The dark region is an elongated crescent-shaped area mostly devoid of emission and located poleward of the main emission dawn arc (Swithenbank-Harris et al., 2019). Around the magnetic pole, the swirl region contains highly variable patchy emissions (Grodent et al., 2003a; Nichols et al., 2009a). Finally, the active region, located between the swirl region and the noon-to-dusk section of the main emission, exhibits a diversity of spots, arcs and diffuse emissions (e.g., Bonfond et al., 2016; Nichols et al., 2017a). Recently, Juno-UVS observations over a large range of local time (LT), including on Jupiter's nightside, showed a strong local-time effect of the most poleward auroral regions (Greathouse et al., 2021). The emissions in the swirl region were observed to be only bright from 5 to 7 LT until 20–22 LT, while they were an order of magnitude weaker at all other local times.

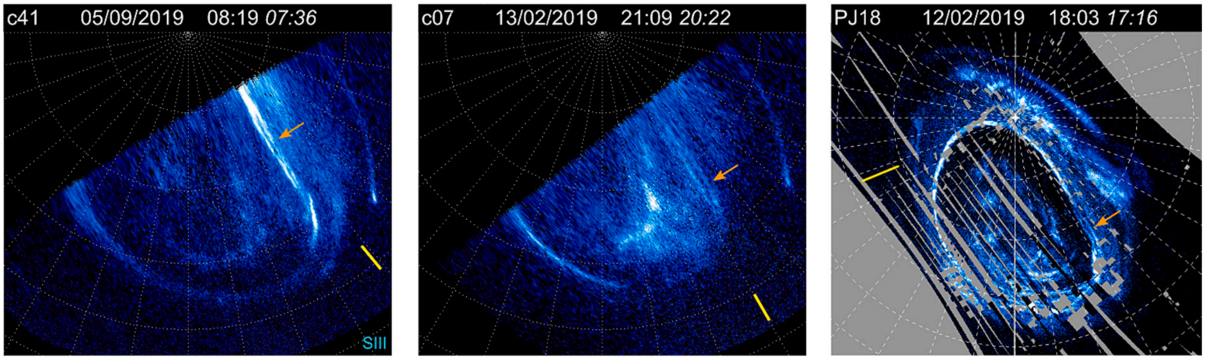

Fig. 7. Examples of the main emissions divided into two narrow parallel arcs (orange arrows) observed by HST (left and middle) and by UVS (right). The yellow line indicates the subsolar longitude. The HST time and the Juno time (in italic) of the observations are indicated. (For interpretation of the references to colour in this figure legend, the reader is referred to the web version of this article.)

4.1. Description of three types of polar brightening

We focus here on three categories of polar emission brightening features frequently observed at Jupiter. In the literature, these three categories are often mixed and grouped under the same name while their characteristics are noticeably different.

The first category consists of polar bright spots. These spots are localized transient brightenings which can appear at any local time

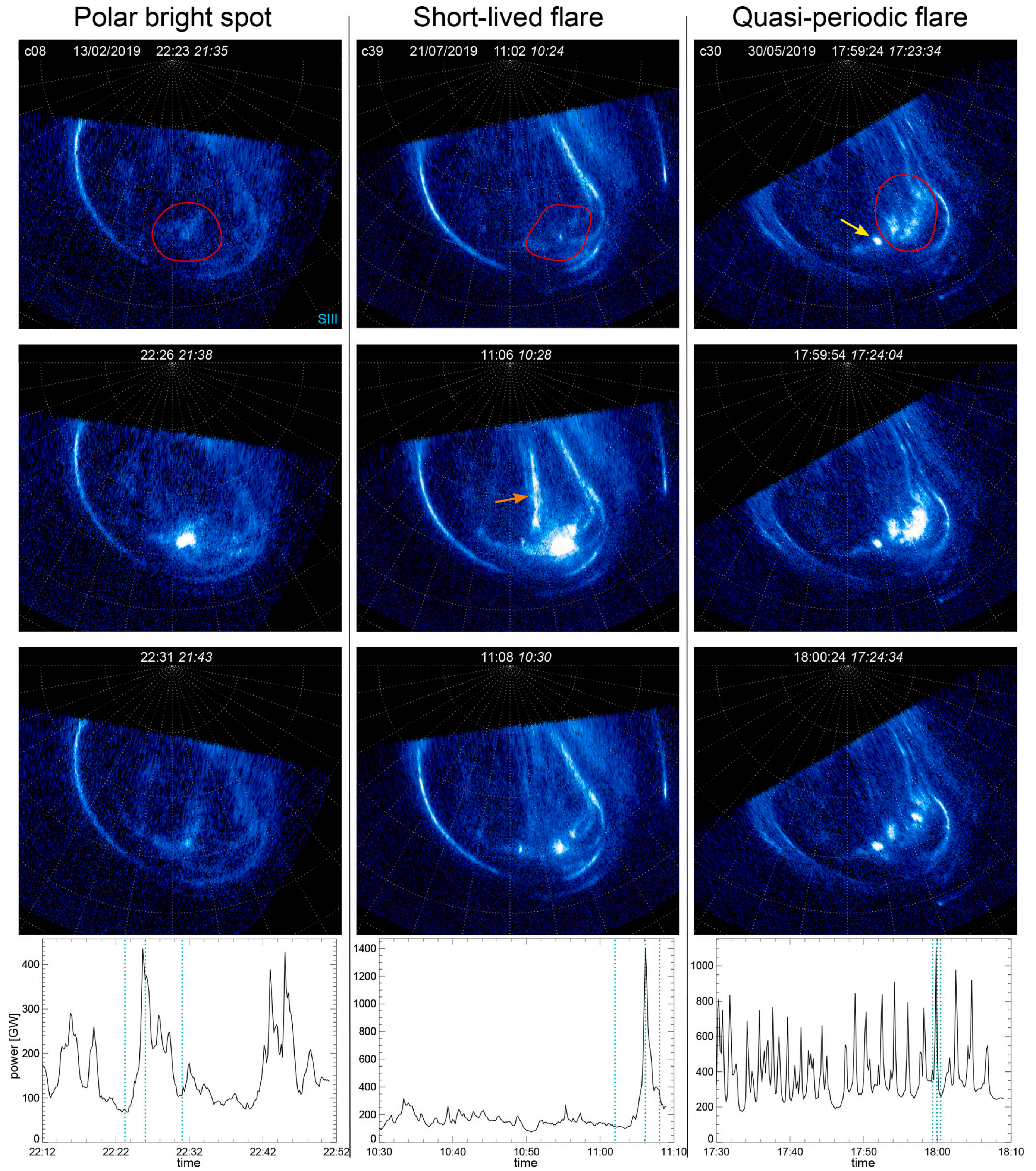

Fig. 8. Observing sequences exhibiting (left) a polar bright spot, (middle) a bright short-lived flare, and (right) a quasi-periodic flare. The HST UT time and the Juno time (in italic) of the observations are indicated on top of each panel. The lower panels show the variation of power inside the region surrounded in red in the upper panels. The vertical dotted lines indicate the time of each HST image in the sequence. The orange arrow points to a transpolar arc and the yellow arrow points to another example of a polar bright spot. (For interpretation of the references to colour in this figure legend, the reader is referred to the web version of this article.)

(feature f in Fig. 3). First reported by Pallier and Prangé (2001, 2004), they have been extensively studied and characterized by Haewsantati et al. (2021) based on Juno-UVS observations. They revealed that the polar bright spots are located at the edge of the swirl region, and they can reappear at nearly the same SIII longitude with a period of 25 min on average and ranging from 3 to 47 min. An example of an HST sequence with a polar bright spot is given in the left column of Fig. 8. The power of the emissions in the region where the bright spot appears (encircled in red) was calculated and its variation throughout the visit is drawn on the lower panel. The times of the three snapshots above are indicated by dotted lines. The whole observing sequence (see Movie S4 in the supplementary material) and the power curve shows that a first small bright spot was present in the same area ~ 11 min earlier and a third one appeared ~17 min later. The polar bright spots are characteristically different from the faint circular expanding auroral features highlighted at the outer edge of the swirl region by Hue et al. (2021a) on Juno-UVS observations. Because of the grazing observing geometry from Earth and their low brightness, these expanding polar features are not observed with HST and are therefore not discussed here, but they could constitute a category of polar emissions on their own.

A second type of polar brightening comprises flares which are very bright emissions lasting a couple of minutes only (Waite et al., 2001; Grodent et al., 2003a). Examples of short-lived flares are indicated by arrows with the letter ‘g’ in Fig. 3. The middle column of Fig. 8 displays another example which also illustrates the lifetime of such an intense flare (Movie S5). The power curve shows the dramatic peak of the power in the region surrounded in red in the first snapshot. The ~minute-long flares occur in the active region and are more extended than the polar bright spots. Their emitted power usually exceeds 1 TW (similar to the typical power emitted by the whole auroral region) and their brightness can peak at a few dozens of MR while the bright spots are generally limited to 5–10 MR. During visit c23, a flare reached the brightness of 56 MR (29 pixels >40 MR, 6 pixels >50 MR), exceeding the precedent record of 37 MR reported by Waite et al. (2001). This flare occurred while the main emission dawn arc was particularly bright. In visit c47, the intense flare (~1.0 TW, peak intensity of ~6.6 MR) indicated by the letter g in Fig. 3 was followed 28 min later by a second flare (~1.2 TW, ~14.7 MR) in the same System III sector. Besides, it should be noted that a polar bright spot and a short-lived flare can coexist, as observed during visit c49 which also exhibits a dawn storm (indicated respectively by the letters f, g and b in Fig. 3).

Simultaneously to the polar flare on c39, the aurora also exhibited a bright and short-lived transpolar arc, also called polar filament, in the swirl region (orange arrow on Fig. 8). This quasi-sun-aligned elongated feature has been reported and described by Nichols et al. (2009a) who concluded that its occurrence is independent of the solar wind conditions and is possibly associated with plasmoids drifting down the magnetotail. These previous observations of transpolar arc do not suggest any correlation with polar flares, though they appeared also at the same time during visit c40 (g and i on Fig. 3). It seems however that the flare brightens all structures of the polar aurora and thus makes the transpolar arc more visible.

A third type of polar activity consists of flashes in the active region, i.e. rapid increase of brightness lasting <30 s (right panels in Fig. 8 and Movie S6). They can continuously recur during the whole visit and they exhibit a quasi-periodicity of a few minutes. Hence, they are often referred to as quasi-periodic flares (Bonfond et al., 2011, 2016). Their brightness peak is however lower than the short-lived flares described earlier, and their characteristic power variation highly differs from both other types of polar activity, as shown in the bottom panels of Fig. 8. In this example, the periodicity inferred from a Lomb-Scargle analysis is 1.8 min. The extension of the quasi-periodic flares is diverse, ranging from a single spot to a large area covering almost the whole active region. Other visits during the campaign show quasi-periodic flares with a reoccurrence time increasing from 2 to 6 min during the visit (c21) and quasi-periodic flashes initiating 20 min after the start of the observations and intensifying towards the end of the sequence (c44, within the frame ‘h’ in Fig. 3). Finally, during c30 (given as an example in Fig. 8), it should be noted that a polar bright spot appears next to the flashing region (yellow arrow).

4.2. Possible generation mechanisms of the polar brightenings

The characteristic morphologies and power variations of the three types of polar emissions depicted here suggest that they are generated by different mechanisms. The source region of the polar bright spots probably corotates with the planet since they can appear several times at the same SIII position during an HST sequence (Haewsantati et al., 2021). Despite being observed at various local times, their initial association with the magnetospheric cusp (Pallier and Prangé, 2001) cannot be dismissed as the cusp morphology can be very complex at Jupiter (Zhang et al., 2021). The quasi-periodic flares occur independently of the solar wind conditions (Bonfond et al., 2016), suggesting an internal driver too. Furthermore, their occurrence in phase in both hemispheres and their mapping strongly indicate that their source region is located on closed field lines crossing the equatorial plane in the outer dayside magnetosphere. However, the synchronized flare brightenings over a large area, sometimes covering the whole active region, suggests that their propagation mechanism lie close to the planet, in the lobes or in the ionosphere (Bonfond et al., 2016).

As mentioned above, the characteristic reoccurrence time of the polar bright spots is tens of minutes (Haewsantati et al., 2021), similar to many quasiperiodic phenomena occurring in the Jovian magnetosphere, with signatures in the plasma measurements (e.g., McKibben et al., 1993; Krupp et al., 2004), radio emissions (e.g., MacDowall et al., 1993; Hospodarsky et al., 2004) and X-Ray aurorae (e.g., Dunn et al., 2016; Wibisono et al., 2020). The characteristic short period of a few minutes of the quasi-periodic flares (Bonfond et al., 2016) has also been identified in radio emissions (Hospodarsky et al., 2004) and particle measurements (McKibben et al., 1993). These periodic phenomena can be explained by the presence of ultralow-frequency waves (ULF), in particular standing Alfvén waves, with periods of 1–60 min, which are found throughout Jupiter’s magnetosphere (Khurana and Kivelson, 1989; Manners and Masters, 2019, 2020). Connections between ULF waves and aurora have been suggested by Nichols et al. (2017b) for a pulsating spot within the main emission and by Pan et al. (2021) who highlighted a positive correlation between the auroral power and the magnetospheric ULF wave power.

Unlike the two other types of polar emissions described here, the short-lived intense flares occurring in the noon active region seem to be an auroral response to solar wind events. They have been interpretated as a consequence of a magnetospheric disturbance caused by a rapid increase of the solar wind dynamic pressure (Waite et al., 2001) or as a signature of sporadic small-scale reconnection at the dayside magnetopause (Grodent et al., 2003a). The intense flare occurring on September 10 (c47, Fig. 3) appears to be preceded by the arrival of a CIR at Jupiter leading to a global brightening of the aurora, as discussed in Section 3.4. However, most of the flares occur while only the dawn arc of the main emission shows high intensities.

We examined at the solar wind propagation models for the flare event occurring on July 21 (Fig. 8). The ENLIL model indicates that a strong CIR hit Jupiter on that day (Fig. S2 middle). Tao’s model shows a quiet solar wind on July 20 and 21 but predicts two successive increases of the SW dynamic pressure on July 22 evening and on July 23 midday (Fig. S1). The geometry between the Earth and Jupiter is favorable for a good prediction but the accuracy on the SW events timing can still be as high as two days. Given the output of the ENLIL simulation, it is then likely that a SW shock reached Jupiter shortly before the intense flare observed on July 21. Finally, according to both solar wind propagation models, a relatively weak CIR arrived at Jupiter ~15-20 h before the extreme flare (~56 MR) occurring at the end of May 22 (Fig. S1 and S2 left).

As they are triggered by solar wind events such as CIRs, the intense flare might preferentially reoccur at the solar period of 25–28 days. This long period cannot be easily identified given the limited HST observations sampling rate and the short lifetime of the flares. We note however that 54 days separate the July 21 flare from the September 13 flare, which corresponds to two solar rotations, and the July 21 flare occurred 60 days after the May 22 flare.

4.3. Bridges

Another auroral feature in the polar region is worth mentioning. It consists of an elongated arc attached to the dusk arc of main emission and curved polewards into the active region. Although often observed, this "bridge" connecting two auroral regions has barely been studied (Pardo Cantos, 2019; Greathouse et al., 2021). Fig. 9 displays some examples of bridges (orange arrows) observed during the campaign. A bright bridge was visible during a short interval of visit c05. Multiple bridges occasionally appear like in visits c01 and c29. The bridges can also pulse, similarly to the quasi-periodic flares found in the active region as well, i.e., with a periodicity of a few minutes. In c01, the bridges a and b have a strikingly similar behavior, pulsing in phase with a similar brightness, while the bridge c has a relatively stable brightness over the visit.

Juno-UVS observations in Fig. 9 were acquired on the same day as visit c29. Both observations show the presence of multiple bridges. Juno provides evidence that the bridges can be found at various longitudes but are always located in the post-noon sector (Greathouse et al., 2021). A dedicated study is required to understand the origin of the bridge feature.

5. Equatorward emissions

5.1. Injection signatures

The emissions equatorward of the main emission include the auroral signatures of injections, the moon auroral footprints and the secondary arc already mentioned in Section 3. Injection signatures are the auroral counterpart of magnetospheric plasma injections (e.g., Mauk et al., 2002; Dumont et al., 2018; Haggerty et al., 2019). They are observed often and consist of emission patches corotating and moving equatorward (features j in Fig. 3). Injection signatures can grow from a dawn storm as they are the consequences of dipolarization following the magnetotail reconnection triggering the dawn storm (Gray et al., 2016; Yao et al., 2020, Bonfond et al., 2021). Such an auroral injection is visible during visit c49 (Fig. 3) and this event was discussed by Yao et al. (2020). Visit c45 provides another example of injection signatures in the postnoon sector (feature j), associated in this case with a pseudo-dawn storm (feature c). Some injection signatures can also develop independently from a dawn storm (e.g., Bonfond et al., 2017b), as it may be the case in visits c40 and c47 (Fig. 3).

5.2. Moon auroral footprints

The HST GO-15683 campaign offers also interesting and diverse observations of the moon auroral footprints. These aurorae are located close to the ionospheric feet of the flux tubes connecting the moons to Jupiter. Io's footprint is the brightest and consists of several distinct spots followed by an extended tail (e.g., Gérard et al., 2006; Bonfond et al., 2008). The Europa and Ganymede footprints generally consist of a unique spot, but a secondary spot is sometimes observed (Bonfond et al., 2013b, 2017a), as well as a short tail (Grodent et al., 2006; Bonfond

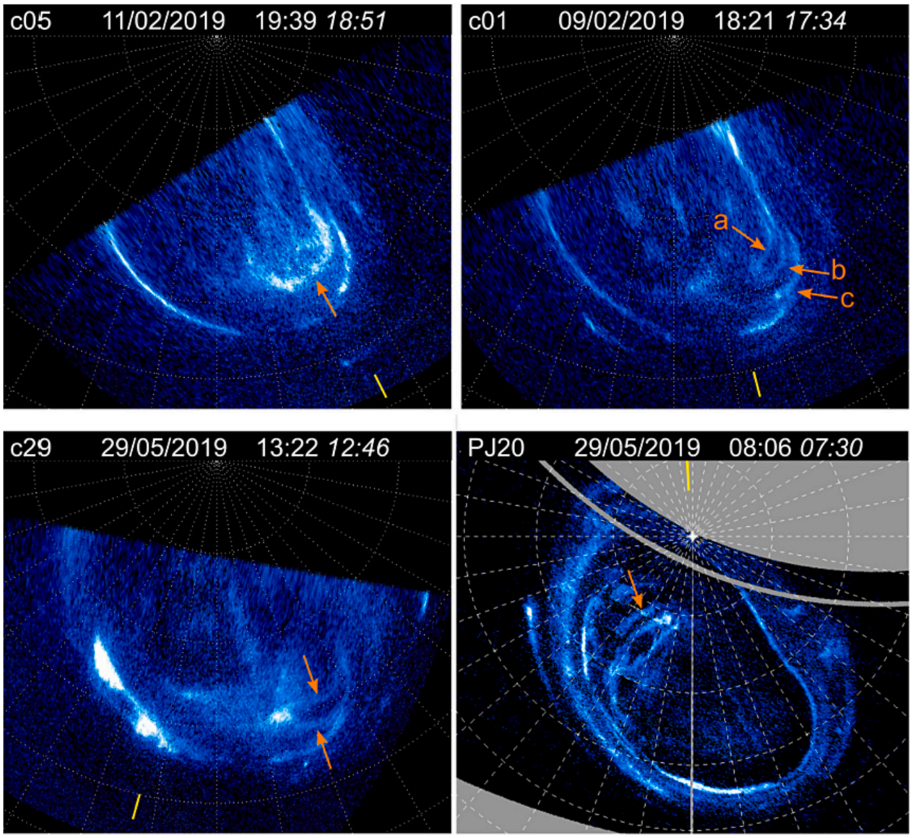

Fig. 9. Examples of the bridge structure (orange arrows) observed by HST and Juno-UVS. The yellow line indicates the subsolar longitude. The HST time and the Juno time (in italic) of the observations are indicated. (For interpretation of the references to colour in this figure legend, the reader is referred to the web version of this article.)

et al., 2017c). Recent Juno infrared observations with a higher spatial resolution revealed that the moon spots and tails have a finer structure made up of several sub-dots (Mura et al., 2018; Moirano et al., 2021).

The characteristics of the moon auroral footprints observed during this campaign, although sometimes particular, are consistent with the generation mechanisms described during the past decade. The moon footprints result from the electromagnetic interaction between the satellites and the magnetospheric plasma rotating rapidly around the planet (Hess et al., 2013a; Bonfond et al., 2013a, 2017a; Hue et al., 2022, 2023 and references therein). The interaction generates Alfvén waves which propagate along the magnetic field lines and are partially reflected by density gradients at the boundaries of the Io plasma torus or of the plasma sheet, or at the Jovian ionosphere. The reflected waves and transhemispheric electron beams generated by the waves produce the multiple spots of the satellite footprints. The tail probably results from multiple reflections of Alfvén waves trapped between density gradients downstream of the satellite (Bonfond et al., 2017c).

Three observing sequences have been selected and are displayed in Fig. 10. The first sequence on the top row shows a bright Io footprint (yellow arrow). The observed maximum brightness of the Io footprint varies by ~50% on timescales of 2–3 min and reaches values up to 16.5 MR during this 2350 s long sequence. Such rapid variations are commonly observed (Bonfond et al. 2007), but the peak brightness is about 3 times brighter than usually observed with Hubble in this longitude range (95–115° SIII) (see Figure 4 in Bonfond et al. 2013) and the Io footprint is brighter than the brightest parts of the main emissions (5.6 MR). The footprint is elongated and the main and secondary spots cannot be disentangled. At these SIII longitudes (~90°), a small inter-spot distance, or even a merging of the spots, is in agreement with the findings of Bonfond et al. (2013a, 2017a) who explain it by Io's location close to the center of the torus. In addition, the position of Io in the dense torus center would lead to more power being generated locally and radiated away in the form of Alfvén waves (Hess et al., 2010, 2013a). The merging of the auroral spots could partly contribute to the enhanced maximum brightness, and the enhanced local interaction in the torus center should lead to a larger total power in the footprint (all spots included). However, these effects alone cannot explain why the Io footprint is so bright in the southern hemisphere around 110° SIII, while the maximum brightness is lower in the northern hemisphere or around 290° in the south, (Bonfond et al., 2013a; Hue et al., 2019b), with Io being in the same position relative to the torus center. The magnetic field strength and the plasma density at various places along the flux

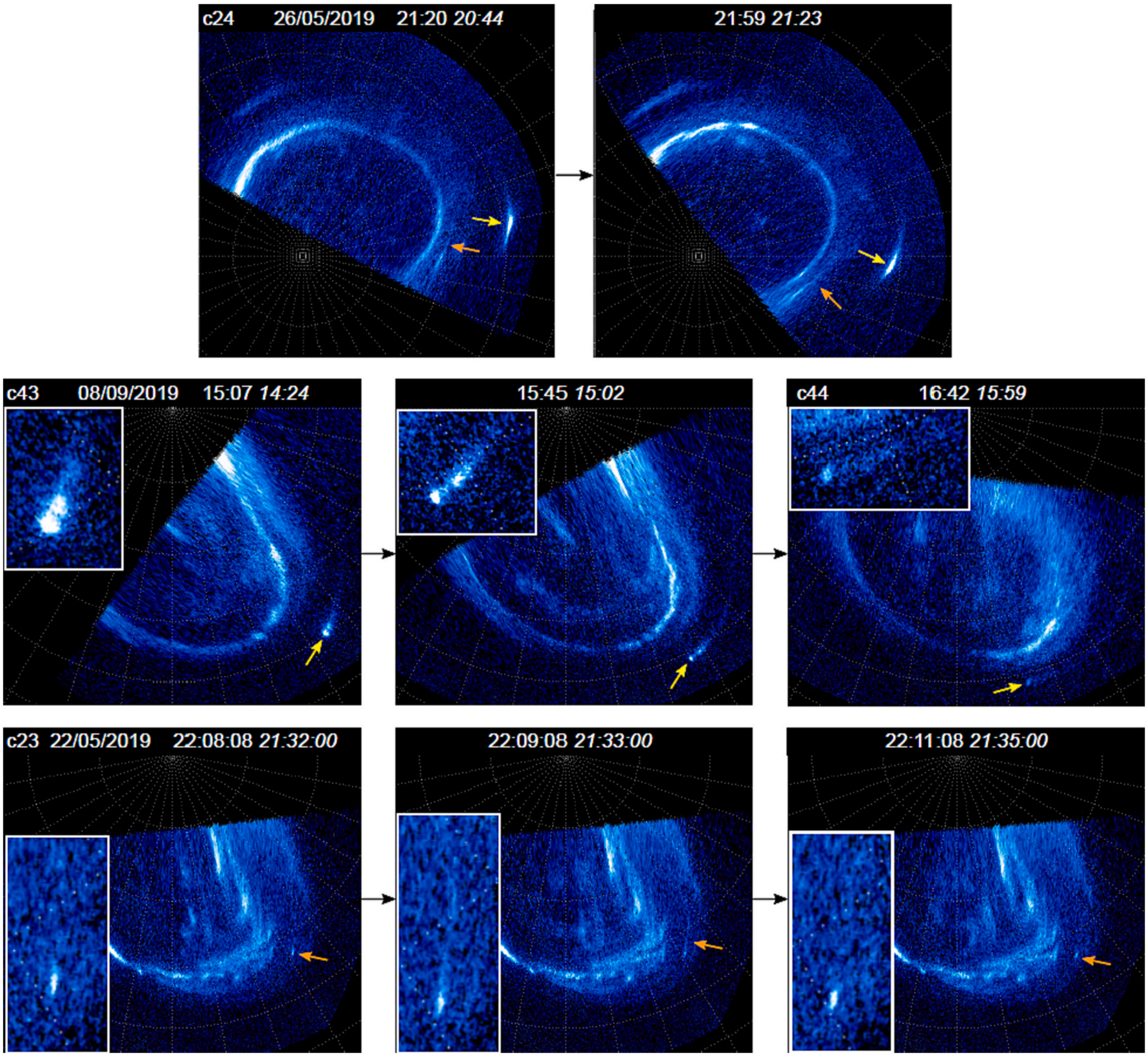

Fig. 10. (Top) Bright Io auroral footprint (yellow arrows) and Ganymede footprint with a tail (orange arrows). (Middle) Evolution of the Io footprint over 1.6 h. A zoom on the footprint is shown on the inset subpanel, with higher saturation. (Bottom) Short-lived tail of the Ganymede footprint. A zoom on the footprint is shown on the inset subpanel, with higher saturation. The HST UT time of the observations are indicated on top of each panel.

tube, influence the partial reflection of the Alfvén waves at the velocity gradients and the efficiency of the Alfvénic electron acceleration (Hess et al., 2013a, 2013b). Further quantitative models would be required to identify the most relevant factors explaining our observations.

The second row of Fig. 10 shows an evolution of the Io footprint. The footprint was bright and a secondary spot trailing the main spot was clearly visible at the start of the observations. The interspot distance was increasing until the end of visit c43. One hour later, on the first image of the next visit (c44), the secondary spot was not present anymore and the main spot was much fainter. The decreasing brightness and the increasing interspot distance from ~145° to 165° SIII longitude are again consistent with the previously published explanations of Io's footprint which predict such variations by the motion of Io inside the plasma torus, going away from the dense torus center (Gérard et al., 2006; Bonfond et al., 2009, 2013a; Wannawichian et al., 2010).

During the observations on top of Fig. 10, a tail can be seen following Ganymede's footprint (orange arrow) during the main part of the visit. Observations of Ganymede footprint tail were surveyed by Bonfond et al. (2017c) and Hue et al. (2023). Its detection with HST is rare since its brightness needs to exceed the outer background emissions and auroral injection signatures found along the Ganymede footprint path. Like for all the previous observations of Ganymede footprint tails, this new observation shows the tail in the 103° - 170° SIII longitude range, where Ganymede moves from the center of the plasma sheet to its northernmost centrifugal latitude (Bonfond et al., 2017c).

Another observation of Ganymede footprint tail is displayed on the last row of Fig. 10. The tail is again found in the same longitudinal sector but contrary to the first example, it was present only during a short time, namely less than three minutes. The rapidity of the appearance and disappearance of such a long coherent structure is noteworthy. Indeed, the footprint tails are thought to stem from multiple Alfvén waves reflections downstream of the moon (Bonfond et al., 2017c), which are phenomena taking several tens of minutes to hours. However, auroral footprint emissions require not only an initial energy source (the local moon-magnetosphere interaction in the equatorial plane), but also favorable conditions for this energy to be reflected or transmitted to higher latitudes and favorable conditions for the acceleration of the charged particles that will precipitate into the atmosphere. Hence the rapid fluctuations of the tail brightness are more likely linked to processes close to the planet than to local perturbations close to the moon. For example, intermittent acceleration structures, called double layers, located around 0.2 R_J above Jupiter's surface, could induce the transient tail appearance. These structures drift away from the planet and disappear after about 10 min (Hess et al., 2009) and are thought to cause short timescale (2–4 min) brightness variations of all three moon footprints (Grodent et al., 2009; Bonfond et al., 2013a, 2017a).

6. Summary

In this manuscript, we gave an overview of the HST campaign GO-15638 and we described several structures observed in the aurora and their dynamical behavior. This campaign shows that the Jovian auroral activity is still high and complex despite taking place during a period near the minimum of solar activity. Although the main emission is often faint, internal magnetospheric processes can brighten it up through, for instance, dawn storms and beads. The combination of HST and Juno-UVS simultaneous observations provided evidence that conjugate dawn storms evolve similarly in both hemispheres. We also highlighted the dynamics within the main emission dawn arc, consisting in its splitting into beads or the merging of beads, which likely reveal plasma instabilities in the plasma sheet. In addition, a long observing sequence showed that a secondary arc parallel to the main emission in the noon-to-dusk local time sector can persist during several days.

Within the dynamic polar aurora, we highlighted the characteristics of three types of emissions. The polar bright spots are localized transient spots which can reappear with a period of tens of minutes. The quasi-periodic flares consist of rapid increase of brightness in the active region, lasting <30 s and with a periodicity of a few minutes. These two types of emissions are internally-driven. Finally, the short-lived flares greatly increase the brightness of the whole polar active region during a few minutes. These powerful flares occur after a CIR hits the magnetosphere. This external disturbance leads also to a brightening of the main emission dawn arc or a global brightening of the whole aurora.

Equatorward of the main emission, new rare observations of the tail of the Ganymede's auroral footprint were reported, one of them showing a tail visible during a very short time. In addition, characteristics of the Io's footprint and their evolution with time prove to be consistent with the observations and theoretical expectations described in the past.

We also highlighted some features which deserve further investigation to be understood, like the elongated arcs connecting the main emission to the polar region, the so-called bridges, in the post-noon sector. In addition, we reported for the first time a splitting of the main emission into two narrow arcs at ~140–150° SIII longitude. This splitting was seen to last for two Jupiter rotations. The current presence of Juno around Jupiter and the wealth of its in situ data, not used here, will definitely help the investigation of the processes generating all these auroral structures.

Supplementary data to this article can be found online at https://doi.org/10.1016/j.icarus.2023.115815.

Declaration of Competing Interest

The authors declare that they have no known competing financial interests or personal relationships that could have appeared to influence the work reported in this paper.

Data availability

The data included herein are based on publicly available observations with the NASA/ESA Hubble Space Telescope (program GO-15638) and obtained at the Space Telescope Science Institute (STScI), which is operated by AURA for NASA (https://archive.stsci.edu/hst/search.php). The Juno-UVS data are archived in NASA's Planetary Data System (http://pds-atmospheres.nmsu.edu/data_and_services/atmospheres_data/JUNO/juno.html).

Acknowledgments

B.P., D.G., B.B. and J.-C.G. acknowledge financial support from the Belgian Federal Science Policy Office (BELSPO) via the PRODEX Programme of ESA. B.B. is a Research Associate of the Fonds de la Recherche Scientifique – FNRS. The work of G.R.G., and T.K.G was funded by NASA's New Frontiers Program for Juno (managed by the Jet Propulsion Laboratory) via a subcontract with Southwest Research Institute. V.H. acknowledges support from the French government under the France 2030 investment plan, as part of the Initiative d'Excellence d'Aix-Marseille Université – A*MIDEX AMX-22-CPJ-04.

References

Badman, S.V., Branduardi-Raymont, G., Galand, M., Hess, S.L., Krupp, N., Lamy, L., Tao, C., 2015. Auroral processes at the giant planets: energy deposition, emission mechanisms, morphology and spectra. Space Sci. Rev. 187, 99–179. https://doi.org/10.1007/s11214-014-0042-x.

Bhardwaj, A., Gladstone, G.R., 2000. Auroral emissions of the giant planets. Rev. Geophys. 38, 295–353. https://doi.org/10.1029/1998rg000046.

Bonfond, B., Grodent, D., Gérard, J.-C., Radioti, A., Saur, J., Jacobsen, S., 2008. UV Io footprint leading spot: a key feature for understanding the UV Io footprint multiplicity? Geophys. Res. Lett. 35, L05107 https://doi.org/10.1029/2007gl032418.

Bonfond, B., Grodent, D., Gérard, J.-C., Radioti, A., Dols, V., Delamere, P.A., Clarke, J.T., 2009. The Io UV footprint: location, inter-spot distances and tail vertical extent. J. Geophys. Res. Space Physics 114, A07224. https://doi.org/10.1029/2009ja014312.

Bonfond, B., Vogt, M.F., Gérard, J.-C., Grodent, D., Radioti, A., Coumans, V., 2011. Quasi-periodic polar flares at Jupiter: a signature of pulsed dayside reconnections? Geophys. Res. Lett. 38, L02104 https://doi.org/10.1029/2010gl045981.

Bonfond, B., Grodent, D., Gérard, J.-C., Stallard, T., Clarke, J.T., Yoneda, M., Gustin, J., 2012. Auroral evidence of Io's control over the magnetosphere of Jupiter. Geophys. Res. Lett. 39, L01105 https://doi.org/10.1029/2011gl050253.

Bonfond, B., Hess, S., Gérard, J.-C., Grodent, D., Radioti, A., Chantry, V., Clarke, J.T., 2013a. Evolution of the Io footprint brightness I: far-UV observations. Planet. Space Sci. 88, 64–75. https://doi.org/10.1016/j.pss.2013.05.023.

Bonfond, B., Hess, S., Bagenal, F., Gérard, J.-C., Grodent, D., Radioti, A., Clarke, J.T., 2013b. The multiple spots of the Ganymede auroral footprint. Geophys. Res. Lett. 40, 4977–4981. https://doi.org/10.1002/grl.50989.

Bonfond, B., Gustin, J., Gérard, J.-C., Grodent, D., Radioti, A., Palmaerts, B., Tao, C., 2015a. The far-ultraviolet main auroral emission at Jupiter - part 1: Dawn-dusk brightness asymmetries. Ann. Geophys. 33, 1203–1209. https://doi.org/10.5194/angeo-33-1203-2015.

Bonfond, B., Gustin, J., Gérard, J.-C., Grodent, D., Radioti, A., Palmaerts, B., Tao, C., 2015b. The far-ultraviolet main auroral emission at Jupiter - part 2: vertical emission profile. Ann. Geophys. 33, 1211–1219. https://doi.org/10.5194/angeo-33-1211-2015.

Bonfond, B., Grodent, D., Badman, S.V., Gérard, J.-C., Radioti, A., 2016. Dynamics of the flares in the active polar region of Jupiter. Geophys. Res. Lett. 43, 11,963–11,970. https://doi.org/10.1002/2016gl071757.

Bonfond, B., Grodent, D., Badman, S.V., Saur, J., Gérard, J.-C., Radioti, A., 2017a. Similarity of the Jovian satellite footprints: spots multiplicity and dynamics. Icarus 292, 208–217. https://doi.org/10.1016/j.icarus.2017.01.009.

Bonfond, B., Gladstone, G.R., Grodent, D., Greathouse, T.K., Versteeg, M.H., Hue, V., Kurth, W.S., 2017b. Morphology of the UV aurorae Jupiter during Juno's first perijove observations. Geophys. Res. Lett. 44, 4463–4471. https://doi.org/10.1002/2017gl073114.

Bonfond, B., Saur, J., Grodent, D., Badman, S.V., Bisikalo, D., Shematovich, V., Radioti, A., 2017c. The tails of the satellite auroral footprints at Jupiter. J. Geophys. Res. Space Physics 122, 7985–7996. https://doi.org/10.1002/2017ja024370.

Bonfond, B., Yao, Z.H., Gladstone, G.R., Grodent, D., Gérard, J.-C., Matar, J., Bolton, S.J., 2021. Are Dawn Storms Jupiter's Auroral Substorms? AGU Adv. 2 https://doi.org/10.1029/2020av000275 e2020AV000275.

Broadfoot, A.L., Belton, M.J., Takacs, P.Z., Sandel, B.R., Shemansky, D.E., Holberg, J.B., McElroy, M.B., 1979. Extreme ultraviolet observations from Voyager 1 encounter with Jupiter. Science 204, 979–982. https://doi.org/10.1126/science.204.4396.979.

Clarke, J. T., Grodent, D., Cowley, S. W., Bunce, E. J., Zarka, P., Connerney, J. E., & Satoh, T. (2004). Jupiter's aurora. Dans F. Bagenal, T. Dowling, & W. McKinnon (Éds.), Jupiter: The Planet, Satellites and Magnetosphere (pp. 639-670). Cambridge Univ. Press.

Chané, E., Palmaerts, B., Radioti, A., 2018. Periodic shearing motions in the Jovian magnetosphere causing a localized peak in the main auroral emission close to noon. Planet. Space Sci. 158, 110–117. https://doi.org/10.1016/j.pss.2018.04.023.

Chané, E., Saur, J., Poedts, S., 2013. Modeling Jupiter's magnetosphere: Influence of the internal sources. J. Geophys. Res. Space Phys. 118, 2157–2172. https://doi.org/10.1002/jgra.50258.

Connerney, J.E., Kotsiaros, S., Oliversen, R.J., Espley, J.R., Joergensen, J.L., Joergensen, P.S., Levin, S.M., 2018. A new model of Jupiter's magnetic field from Juno's first nine orbits. Geophys. Res. Lett. 45, 2590–2596. https://doi.org/10.1002/2018gl077312.

Dumont, M., Grodent, D., Radioti, A., Bonfond, B., Roussos, E., Paranicas, C., 2018, October. Evolution of the Auroral signatures of Jupiter's Magnetospheric injections. J. Geophys. Res. Space Physics 123, 8489–8501. https://doi.org/10.1029/2018ja025708.

Dunn, W.R., Branduardi-Raymont, G., Elsner, R.F., Vogt, M.F., Lamy, L., Ford, P.G., Jasinski, J.M., 2016. The impact of an ICME on the Jovian X-ray aurora. J. Geophys. Res. Space Physics 121, 2274–2307. https://doi.org/10.1002/2015ja021888.

Gérard, J.C., Gkouvelis, L., Bonfond, B., Grodent, D., Gladstone, G.R., Hue, V., et al., 2020. Spatial distribution of the Pedersen conductance in the Jovian Aurora from Juno-UVS spectral images. J. Geophys. Res. Space Physics 125 (8). https://doi.org/10.1029/2020JA028142 e2020JA028142.

Gérard, J.-C., Saglam, A., Grodent, D., Clarke, J.T., 2006. Morphology of the ultraviolet Io footprint emission and its control by Io's location. J. Geophys. Res. 111, A04202 https://doi.org/10.1029/2005ja011327.

Gérard, J.-C., Bonfond, B., Grodent, D., Radioti, A., 2016. The color ratio-intensity relation in the Jovian aurora: Hubble observations of auroral components. Planet. Space Sci. 131, 14–23. https://doi.org/10.1016/j.pss.2016.06.004.

Gladstone, G.R., Persyn, S.C., Eterno, J.S., Walther, B.C., Slater, D.C., Davis, M.W., Denis, F., 2017. The ultraviolet spectrograph on NASA's Juno Mission. Space Sci. Rev. 213, 447–473. https://doi.org/10.1007/s11214-014-0040-z.

Gray, R.L., Badman, S.V., Bonfond, B., Kimura, T., Misawa, H., Nichols, J.D., Ray, L.C., 2016. Auroral evidence of radial transport at Jupiter during January 2014. J. Geophys. Res. Space Phys. 121, 9972–9984. https://doi.org/10.1002/2016ja023007.

Gray, R.L., Badman, S.V., Woodfield, E.E., Tao, C., 2017. Characterization of Jupiter's secondary auroral oval and its response to hot plasma injections. J. Geophys. Res. Space Physics 122, 6415–6429. https://doi.org/10.1002/2017ja024214.

Greathouse, T., Gladstone, R., Versteeg, M., Hue, V., Kammer, J., Giles, R., Vogt, M.F., 2021. Local time dependence of Jupiter's polar auroral emissions observed by Juno UVS. J. Geophys. Res.: Planets 126. https://doi.org/10.1029/2021je006954 e2021JE006954.

Greathouse, T.K., Gladstone, G.R., Davis, M.W., Slater, D.C., Versteeg, M.H., Persson, K. B., et al., 2013. Performance Results from in-flight Commissioning of the Juno Ultraviolet Spectrograph (Juno-UVS). In: Proceedings UV, X-Ray, and Gamma-Ray Space Instrumenta- tion for Astronomy XVIII. (Vol. 8859, p. 88590T). International Society for Optics and Photonics.

Grodent, D., Clarke Jr., J.T., J. H, Cowley, S.W., Gérard, J.-C., Kim, J., 2003a. Jupiter's polar auroral emissions. J. Geophys. Res. 108, 1366. https://doi.org/10.1029/2003ja010017.

Grodent, D., Clarke, J.T., Kim Jr., J., J. H, Cowley, S.W., 2003b. Jupiter's main auroral oval observed with HST-STIS. J. Geophys. Res. 108, 1389. https://doi.org/10.1029/2003ja009921.

Grodent, D., Gérard, J.-C., Gustin, J., Mauk, B.H., Connerney, J.E., Clarke, J.T., 2006. Europa's FUV auroral tail on Jupiter. Geophys. Res. Lett. 33, L06201 https://doi.org/10.1029/2005gl025487.

Grodent, D., Bonfond, B., Gérard, J.-C., Radioti, A., Gustin, J., Clarke, J.T., Nichols, J., 2008. Auroral evidence of a localized magnetic anomaly in Jupiter's northern hemisphere. J. Geophys. Res. 113, A09201. https://doi.org/10.1029/2008JA013185.

Grodent, D., Bonfond, B., Radioti, A., Gérard, J.-C., Jia, X., Nichols, J.D., Clarke, J.T., 2009. Auroral footprint of Ganymede. J. Geophys. Res. 114, A07212 https://doi.org/10.1029/2009ja014289.

Grodent, D., Bonfond, B., Yao, Z., Gérard, J.-C., Radioti, A., Dumont, M., Valek, P., 2018. Jupiter's Aurora observed with HST during Juno orbits 3 to 7. J. Geophys. Res. Space Physics 123, 3299–3319. https://doi.org/10.1002/2017ja025046.

Guo, R.L., Yao, Z.H., Dunn, W.R., Palmaerts, B., Sergis, N., Grodent, D., Dougherty, M.K., 2021. A rotating azimuthally distributed Auroral current system on Saturn revealed by the Cassini spacecraft. Astrophys. J. Lett. 919, L25. https://doi.org/10.3847/2041-8213/ac26b5.

Gustin, J., Bonfond, B., Grodent, D., Gérard, J.-C., 2012. Conversion from HST ACS and STIS auroral counts into brightness, precipitated power, and radiated power for H2 giant planets. J. Geophys. Res. Space Physics 117, A07316. https://doi.org/10.1029/2012ja017607.

Haewsantati, K., Bonfond, B., Wannawichian, S., Gladstone, G.R., Hue, V., Versteeg, M. H., Vogt, M.F., 2021. Morphology of Jupiter's Polar Auroral bright spot emissions via Juno-UVS observations. J. Geophys. Res. Space Physics 126. https://doi.org/10.1029/2020ja028586 e2020JA028586.

Haggerty, D.K., Mauk, B.H., Paranicas, C.P., Clark, G., Kollmann, P., Rymer, A.M., Levin, S.M., 2019. Jovian injections observed at high latitude. Geophys. Res. Lett. 46, 9397–9404. https://doi.org/10.1029/2019gl083442.

Hess, S., Zarka, P., Mottez, F., Ryabov, V.B., 2009. Electric potential jumps in the Io-Jupiter flux tube. Planet. Space Sci. 57, 23–33. https://doi.org/10.1016/j.pss.2008.10.006.

Hess, S.L., Delamere, P., Dols, V., Bonfond, B., Swift, D., 2010. Power transmission and particle acceleration along the Io flux tube. J. Geophys. Res. 115, A06205 https://doi.org/10.1029/2009ja014928.

Hess, S.L., Bonfond, B., Chantry, V., Gérard, J.-C., Grodent, D., Jacobsen, S., Radioti, A., 2013a. Evolution of the Io footprint brightness II: modeling. Planet. Space Sci. 88, 76–85. https://doi.org/10.1016/j.pss.2013.08.005.

Hess, S.L.G., Bonfond, B., Delamere, P.A., 2013b. How could the Io footprint disappear? Planet. Space Sci. 89, 102–110. https://doi.org/10.1016/j.pss.2013.08.014.

Hospodarsky, G.B., Kurth, W.S., Cecconi, B., Gurnett, D.A., Kaiser, M.L., Desch, M.D., Zarka, P., 2004. Simultaneous observations of Jovian quasi-periodic radio emissions by the Galileo and Cassini spacecraft. J. Geophys. Res. 109, A09S07. https://doi.org/10.1029/2003JA010263.

Hue, V., Gladstone, G.R., Greathouse, T.K., Kammer, J.A., Davis, M.W., Bonfond, B., et al., 2019a. In-flight characterization and calibration of the Juno ultraviolet spectrograph (Juno-UVS). Astron. J. 157, 90. https://doi.org/10.3847/1538-3881/aafb36.

Hue, V., Greathouse, T.K., Bonfond, B., Saur, J., Gladstone, G.R., Roth, L., et al., 2019b. Juno-UVS observation of the Io footprint during solar eclipse. J. Geophys. Res. Space Physics 124 (7), 5184–5199. https://doi.org/10.1029/2018JA026431.

Hue, V., Greathouse, T.K., Gladstone, G.R., Bonfond, B., Gérard, J.-C., Vogt, M.F., Connerney, J.E., 2021a. Detection and characterization of circular expanding UV-emissions observed in Jupiter's Polar Auroral regions. J. Geophys. Res. Space Physics 126. https://doi.org/10.1029/2020ja028971 e2020JA028971.

Hue, V., Giles, R.S., Gladstone, G.R., Greathouse, T.K., Davis, M.W., Kammer, J.A., Versteeg, M.H., 2021b. Updated radiometric and wavelength calibration of the Juno ultraviolet spectrograph. J. Astron. Telescop. Instr. Syst. 7, 044003 https://doi.org/10.1117/1.JATIS.7.4.044003.

Hue, V., Szalay, J.R., Greathouse, T.K., Bonfond, B., Kotsiaros, S., Louis, C.K., Mauk, B.H., 2022. A comprehensive set of Juno in situ and remote sensing observations of the ganymede auroral footprint. Geophys. Res. Lett. 49 https://doi.org/10.1029/2021gl096994 e2021GL096994.

Hue, V., Gladstone, G.R., Louis, C.K., Greathouse, T.K., Bonfond, B., Szalay, J.R., Connerney, J.E.P., 2023. The Io, Europa, and Ganymede auroral footprints at Jupiter in the Ultraviolet: Positions and equatorial lead angles. J. Geophys. Res. Space Physics 128. https://doi.org/10.1029/2023JA031363 e2023JA031363.

Kalmoni, N.M., Rae, I.J., Watt, C.E., Murphy, K.R., Forsyth, C., Owen, C.J., 2015. Statistical characterization of the growth and spatial scales of the substorm onset arc. J. Geophys. Res. Space Physics 120, 8503–8516. https://doi.org/10.1002/2015ja021470.

Khurana, K.K., Kivelson, M.G., 1989. Ultralow frequency MHD waves in Jupiter's middle magnetosphere. J. Geophys. Res. 94, 5241–5254. https://doi.org/10.1029/ja094ia05p05241.

Kimura, T., Badman, S.V., Tao, C., Yoshioka, K., Murakami, G., Yamazaki, A., Clarke, J. T., 2015. Transient internally driven aurora at Jupiter discovered by Hisaki and the

Hubble Space Telescope. Geophys. Res. Lett. 42, 1662–1668. https://doi.org/10.1002/2015gl063272.

Kimura, T., Nichols, J.D., Gray, R.L., Tao, C., Murakami, G., Yamazaki, A., Fujimoto, M., 2017. Transient brightening of Jupiter's aurora observed by the Hisaki satellite and Hubble Space Telescope during approach phase of the Juno spacecraft. Geophys. Res. Lett. 44, 4523–4531. https://doi.org/10.1002/2017gl072912.

Kimura, T., Hiraki, Y., Tsuchya, F., Delamere, P.A., Yoshioka, K., Murakami, G., Fujimoto, M., 2018. Response of Jupiter's aurora to plasma mass loading rate monitored by the Hisaki satellite during volcamic eruptions at Io. J. Geophys. Res. Space Physics 123, 1885–1899. https://doi.org/10.1002/2017JA025029.

Kita, H., Kimura, T., Tao, C., Tsuchiya, F., Murakami, G., Yamazaki, A., Fujimoto, M., 2019. Jovian UV Aurora's response to the solar wind: Hisaki EXCEED and Juno observations. J. Geophys. Res. Space Physics 124, 10,209–10,218. https://doi.org/10.1029/2019ja026997.

Krupp, N., Woch, J., Lagg, A., Livi, S., Mitchell, D.G., Krimigis, S.M., Espinosa, S.A., 2004. Energetic particle observations in the vicinity of Jupiter: Cassini MIMI/LEMMS results. J. Geophys. Res. 109, A09S10. https://doi.org/10.1029/2003JA010111.

MacDowall, R.J., Kaiser, M.L., Desch, M.D., Farrell, W.M., Hess, R.A., Stone, R.G., 1993. Quasiperiodic Jovian radio bursts: observations from the Ulysses Radio and plasma wave experiment. Planet. Space Sci. 41, 1059–1072.

Manners, H., Masters, A., 2019. First evidence for multiple-harmonic standing Alfvén waves in Jupiter's equatorial plasma sheet. Geophys. Res. Lett. 46, 9344–9351. https://doi.org/10.1029/2019gl083899.

Manners, H., Masters, A., 2020. The global distribution of ultralow-frequency waves in Jupiter's magnetosphere. J. Geophys. Res. Space Physics 125. https://doi.org/10.1029/2020ja028345 e2020JA028345.

Mauk, B.H., Clarke, J.T., Grodent, D., Waite, J.H., Paranicas, C.P., Williams, D.J., 2002. Transient aurora on Jupiter from injections of magnetospheric electrons. Nature 415, 1003–1005. https://doi.org/10.1038/4151003a.

McKibben, R.B., Simpson, J.A., Zhang, M., 1993. Impulsive bursts of relativistic electrons discovered during Ulysses' traversal of Jupiter's dusk-side magnetosphere. Planet. Space Sci. 41, 1041–1058. https://doi.org/10.1016/0032-0633(93)90108-E.

Moirano, A., Mura, A., Adriani, A., Dols, V., Bonfond, B., Waite, J.H., Bolton, S.J., 2021. Morphology of the Auroral Tail of Io, Europa, and Ganymede From JIRAM L-Band Imager. J. Geophys. Res. Space Physics 126. https://doi.org/10.1029/2021ja029450 e2021JA029450.

Mura, A., Adriani, A., Connerney, J.E., Bolton, S., Altieri, F., Bagenal, F., Turrini, D., 2018. Juno observations of spot structures and a split tail in Io-induced aurorae on Jupiter. Science 361, 774–777. https://doi.org/10.1126/science.aat1450.

Nichols, J.D., Bunce, E.J., Clarke, J.T., Cowley, S.W., Gérard, J.-C., Grodent, D., Pryor, W. R., 2007. Response of Jupiter's UV auroras to interplanetary conditions as observed by the Hubble Space Telescope during the Cassini flyby campaign. J. Geophys. Res. Space Physics 112, A02203. https://doi.org/10.1029/2006ja012005.

Nichols, J.D., Clarke, J.T., Gérard, J.C., Grodent, D., 2009a. Observations of Jovian polar auroral filaments. Geophys. Res. Lett. 36, L08101 https://doi.org/10.1029/2009gl037578.

Nichols, J.D., Clarke, J.T., Gérard, J.C., Grodent, D., Hansen, K.C., 2009b. Variation of different components of Jupiter's auroral emission. J. Geophys. Res. Space Physics 114, A06210. https://doi.org/10.1029/2009ja014051.

Nichols, J.D., Badman, S.V., Bagenal, F., Bolton, S.J., Bonfond, B., Bunce, E.J., Yoshikawa, I., 2017a. Response of Jupiter's auroras to conditions in the interplanetary medium as measured by the Hubble space telescope and Juno. Geophys. Res. Lett. 44, 7643–7652. https://doi.org/10.1002/2017gl073029.

Nichols, J.D., Yeoman, T.K., Bunce, E.J., Chowdhury, M.N., Cowley, S.W., Robinson, T. R., 2017b. Periodic emission within Jupiter's Main Auroral oval. Geophys. Res. Lett. 44, 9192–9198. https://doi.org/10.1002/2017gl074824.

Nichols, J.D., Kamran, A., Milan, S.E., 2019. Machine learning analysis of Jupiter's far-ultraviolet Auroral morphology. J. Geophys. Res. Space Physics 124, 8884–8892. https://doi.org/10.1029/2019ja027120.

Odstrcil, D., 2003. Modeling 3-D solar wind structure. Adv. Space Res. 32, 497–506. https://doi.org/10.1016/s0273-1177(03)00332-6.

Odstrcil, D., Riley, P., Zhao, X.P., 2004. Numerical simulation of the 12 May 1997 interplanetary CME event. J. Geophys. Res. 109, A02116 https://doi.org/10.1029/2003ja010135.

Pallier, L., Prangé, R., 2001. More about the structure of the high latitude Jovian aurorae. Planet. Space Sci. 49, 1159–1173. https://doi.org/10.1016/s0032-0633(01)00023-x.

Pallier, L., Prangé, R., 2004. Detection of the southern counterpart of the Jovian northern polar cusp: shared properties. Geophys. Res. Lett. 31, L06701 https://doi.org/10.1029/2003gl018041.

Palmaerts, B., Radioti, A., Grodent, D., Chané, E., Bonfond, B., 2014. Transient small-scale structure in the main auroral emission at Jupiter. J. Geophys. Res. Space Physics 119, 9931–9938. https://doi.org/10.1002/2014ja020688.

Pan, D.-X., Yao, Z.-H., Manners, H., Dunn, W., Bonfond, B., Grodent, D., Wei, Y., 2021. Ultralow-frequency waves in driving Jovian Aurorae revealed by observations from HST and Juno. Geophys. Res. Lett. 48 https://doi.org/10.1029/2020gl091579 e2020GL091579.

Pardo Cantos, I., 2019. A new auroral structure on Jupiter: Jupiter's auroral bridge. Master's Thesis. University of Liege, Belgium. Récupéré sur. http://hdl.handle.net/2268.2/7581.

Pu, Z.Y., Korth, A., Chen, Z.X., Friedel, R.H., Zong, Q.G., Wang, X.M., Pulkkinen, T.I., 1997. MHD drift ballooning instability near the inner edge of the near-earth plasma sheet and its application to substorm onset. J. Geophys. Res. 102, 14397–14406. https://doi.org/10.1029/97ja00772.

Radioti, A., Gérard, J.-C., Grodent, D., Bonfond, B., Krupp, N., Woch, J., 2008. Discontinuity in Jupiter's main auroral oval. J. Geophys. Res. Space Physics 113, A01215. https://doi.org/10.1029/2007ja012610.

Radioti, A., Yao, Z., Grodent, D., Palmaerts, B., Roussos, E., Dialynas, K., Bonfond, B., 2019. Auroral beads at Saturn and the driving mechanism: Cassini proximal orbits. Astrophys. J. 885, L16. https://doi.org/10.3847/2041-8213/ab4e20.

Rae, I.J., Watt, C.E., Mann, I.R., Murphy, K.R., Samson, J.C., Kabin, K., Angelopoulos, V., 2010. Optical characterization of the growth and spatial structure of a substorm onset arc. J. Geophys. Res. 115, A10222 https://doi.org/10.1029/2010ja015376.

Swithenbank-Harris, B.G., Nichols, J.D., Bunce, E.J., 2019. Jupiter's dark polar region as observed by the Hubble Space Telescope during the Juno approach phase. J. Geophys. Res. Space Physics 124, 9094–9105. https://doi.org/10.1029/2019ja027306.

Swithenbank-Harris, B.G., Nichols, J.D., Allegrini, F., Bagenal, F., Bonfond, B., Bunce, E. J., Wilson, R.J., 2021. Simultaneous observation of an Auroral Dawn storm with the Hubble Space Telescope and Juno. J. Geophys. Res. Space Physics 126. https://doi.org/10.1029/2020ja028717 e2020JA028717.

Tao, C., Kataoka, R., Fukunishi, H., Takahashi, Y., Yokoyama, T., 2005. Magnetic field variations in the Jovian magnetotail induced by solar wind dynamic pressure enhancements. J. Geophys. Res. 110, A11208 https://doi.org/10.1029/2004ja010959.

Tao, C., Kimura, T., Tsuchiya, F., Muirakami, G., Yoshioka, K., Yamakazi, A., Fujimoto, M., 2018. Variation of Jupiter's aurora observed by Hisaki/EXCEED: 3. Volcanic control of Jupiter's Aurora. Geophys. Res. Lett. 45, 71–79. https://doi.org/10.1002/2017GL075814.

Tomás, A.T., Woch, J., Krupp, N., Lagg, A.K., Glassmeier, H., Kurth, W.S., 2004. Energetic electrons in the inner part of the Jovian magnetosphere and their relation to auroral emissions. J. Geophys. Res. 109, A06203 https://doi.org/10.1029/2004ja010405.

Waite, J.H., Gladstone, G.R., Lewis, W.S., Goldstein, R., McComas, D.J., Riley, P., Young, D.T., 2001. An auroral flare at Jupiter. Nature 410, 787–789. https://doi.org/10.1038/35071018.

Wannawichian, S., Clarke, J.T., Nichols, J.D., 2010. Ten years of Hubble Space Telescope observations of the variation of the Jovian satellites' auroral footprint brightness. J. Geophys. Res. 115, A02206 https://doi.org/10.1029/2009ja014456.

Wibisono, A.D., Branduardi-Raymont, G., Dunn, W.R., Coates, A.J., Weigt, D.M., Jackman, C.M., Fleming, D., 2020. Temporal and spectral studies by XMM-Newton of Jupiter's X-ray Auroras during a compression event. J. Geophys. Res. Space Physics 125. https://doi.org/10.1029/2019ja027676 e2019JA027676.

Yao, Z., Pu, Z.Y., Rae, I.J., Radioti, A., Kubyshkina, M.V., 2017. Auroral streamer and its role in driving wave-like pre-onset aurora. Geosci. Lett. 4 https://doi.org/10.1186/s40562-017-0075-6.

Yao, Z.H., Bonfond, B., Clark, G., Grodent, D., Dunn, W.R., Vogt, M.F., Bolton, S.J., 2020. Reconnection- and Dipolarization-Driven Auroral Dawn Storms and injections. J. Geophys. Res. Space Physics 125. https://doi.org/10.1029/2019ja027663 e2019JA027663.

Yao, Z.H., Bonfond, B., Grodent, D., Chané, E., Dunn, W.R., Kurth, W.S., Bolton, S.J., 2022. On the relation between auroral morphologies and compression conditions of Jupiter's magnetopause: observations from Juno and the Hubble Space Telescope. J. Geophys. Res. Space Physics 127. https://doi.org/10.1029/2021JA029894 e2021JA029894.

Yoshikawa, I., Suzuki, F., Hikida, R., Yoshioka, K., Murakami, G., Tsuchiya, F., Fujimoto, M., 2017. Volcanic activity on Io and its influence on the dynamics of the Jovian magnetosphere observed by EXCEED/Hisaki in 2015. Earth Planets Space 69. https://doi.org/10.1186/s40623-017-0700-9.

Yung, Y.L., Gladstone, G.R., Chang, K.M., Ajello, J.M., Srivastava, S.K., 1982. H2 fluorescence spectrum from 1200 to 1700 a by electron impact - laboratory study and application to Jovian aurora. Astrophys. J. 254, L65–L69. https://doi.org/10.1086/183757.

Zhang, B., Delamere, P.A., Yao, Z., Bonfond, B., Lin, D., Sorathia, K.A., Lyon, J.G., 2021. How Jupiter's unusual magnetospheric topology structures its aurora. Sci. Adv. 7, eabd1204. https://doi.org/10.1126/sciadv.abd1204.